

UVM ScholarWorks

Deconvolving Maps of Intra-Cardiac Electrical Potential

Item Type	thesis;article
Authors	Palmer, Keryn
Download date	2026-06-12 08:56:55
Link to Item	https://hdl.handle.net/20.500.14849/3688

**DECONVOLVING MAPS OF INTRA-CARDIAC ELECTRICAL
POTENTIAL**

A Thesis Presented

by

Keryn Palmer

to

The Faculty of the Graduate College

of

The University of Vermont

**In Partial Fulfillment of the Requirements
for the Degree of Master of Science
Specializing in Biomedical Engineering**

May, 2012

Abstract

Atrial fibrillation (AF) is the most common arrhythmia encountered in clinical practice, occurring in 1% of the adult population of North America. Although AF does not typically lead to risk of immediate mortality, it is a potent risk factor for ischemic stroke. When left untreated AF reduces quality of life, functional status, cardiac performance and is associated with higher medical costs and an increased risk of death. Catheter ablation is a commonly used treatment method for those who suffer from drug-refractory AF. Prior to ablation, intra-cardiac mapping can be used to determine the activation sequence of cardiac tissue, which may be useful in deciding where to place ablation lesions. However, the electrical potential that is recorded during mapping is not a direct reflection of the current density across the tissue because the potential recorded at each point above the heart tissue is influenced by every cell in the tissue. This causes the recorded potential to be a blurred version of the true tissue current density. The potential that is observed can be described as the convolution of the true current density with a point spread function. Accordingly, deconvolution can, in principle, be used in order to improve the resolution of potential maps. However, because the number of electrodes which can be deployed transvenously is limited by practical restrictions, the recorded potential field is a sparsely sampled version of the actual potential field. Further, an electrode array cannot sample over the entire atrial surface, so the potential map that is observed is a truncated version of the global electrical activity. Here, we investigate the effects of electrode sampling density and edge extension on the ability of deconvolution to improve the resolution of measured electrical potentials within the atria of the heart. In particular, we identify the density of sensing electrodes that are required to allow deconvolution to provide improved estimation of the true current density when compared to the observed potential field.

Acknowledgements

I would like to give my thanks to several individuals who have been essential to my completion of this project and to the production of this document. I would like to thank the members of my thesis committee for their guidance and support throughout the project. A great deal of gratitude is due to my research advisor, Dr. Bates, for his guidance, teaching, and commitment to my scientific growth. Special thanks are also due to Dr. Spector who has played a crucial role in providing an understanding of clinical and simulated physiology and implications of my findings. All of my committee members have supported and enabled my pursuit of knowledge in both engineering and medicine, providing support for my academic accomplishments and playing an invaluable role in making my experience at the University of Vermont enjoyable and academically rewarding.

Special thanks are also due to the scientists and students working in the labs of Dr. Bates and Dr. Spector who have provided feedback and a great deal of help throughout my completion of this project. Finally, I would like to thank my family and friends who have supported me throughout my academic endeavors; this would have been impossible without you.

Table of Contents

Acknowledgements.....	ii
List of Figures.....	v
Chapter One: Introduction	1
Chapter Two: Background.....	4
2.1 Physiology.....	4
2.1.1 Atrial Fibrillation	4
2.2 Treatment Methods.....	6
2.2.1 Anti-arrhythmic Drug Therapy	6
2.2.2 Catheter Ablation.....	7
2.2.3 Mapping Techniques.....	9
2.3 Deconvolution Theory	11
2.3.1 Convolution and Deconvolution.....	11
2.3.2 Fourier Transform.....	12
2.3.3 Effects of Noise.....	15
2.3.4 Data Truncation	15
2.4 Simulation of Atrial Activation	16
Chapter Three: Deconvolution in One Dimension.....	19
3.1 Background.....	19
3.2 Computational Methods.....	19
3.3 Results.....	24
3.3.1 Effects of Electrode Array Size	24
3.3.2 Effects of Electrode Height.....	26
3.4 Discussion.....	28
Chapter Four: Deconvolution in Two Dimensions.....	31
4.1 Background.....	31
4.2 Computational Methods.....	31
4.3 Results.....	37
4.3.1 Effects of Electrode Array Size	37
4.3.2 Effects of Electrode Height.....	44
4.3.3 Effects of Edge Extension.....	47
4.4 Discussion.....	49
Chapter Five: Conclusions.....	56

References.....	58
Appendices.....	61
A. One Dimensional Deconvolution Code	61
B. Two Dimensional Deconvolution Code.....	64

List of Figures

Figure 1. Normal electrical conduction in the heart (left), and disorganized conduction as is seen during atrial fibrillation (right).....	5
Figure 2. Ablation encircling the pulmonary veins on both sides of the atrium as shown by Ames et al[7].....	8
Figure 3. Reentry shown in a physiologically realistic model as is seen in the model created by Vigmond et al [15].	17
Figure 4. Reentry secondary to fixed, anatomic substrate, as seen in the model by Spector et al [43]	18
Figure 5. Example of the current density - $I(z, t)$	20
Figure 6. Example of the convolved signal, $\Phi(x)$, which consists of the current density convolved with the point spread function.	21
Figure 7. Example of the cubic spline interpolation (shown in pink) found using 50 electrodes to sample the convolved signal.....	22
Figure 8. Images showing the deconvolved signal (blue) the convolved signal (pink) and the true signal (black) at electrode spacing of 4 (a) and 40 (b).....	25
Figure 9. Mean squared residual values of the deconvolved and observed signals varying electrode spacing with electrode height of 25 (a) and 150 (b).....	26
Figure 10. MSR calculated when the electrode location is shifted by 1.....	27
Figure 11. The mean squared residual value calculated between the "true signal" and the convolved signal becomes increasingly large as the electrode height is increased.	28
Figure 12. Example of the true current density field $I(z, w, h)$	33
Figure 13. Example of an interpolated convolved signal with an electrode spacing of 15.	33
Figure 14. The window used to smoothly extend the convolved signal.	34
Figure 15. Example of a truncated convolved signal (a), smooth edge extension applied to the signal (b), and the extended signal multiplied by our window (c).....	35

Figure 16. True current density, observed electrical potential, and deconvolved signal at multiple time steps using an electrode array of 20 x 20 (a) and 10 x 10 (b) at a height of 2.	39
Figure 17. True current density, observed signal, and deconvolved signal using a 30 x 30 and 15 x 15 array of electrodes at a height of 2.	41
Figure 18. MSR comparing the observed and deconvolved signal with the true signal... 42	
Figure 19. MSR comparing the observed and deconvolved signal with the true signal.. 43	
Figure 20. Observed signal at heights of 1, 5, and 10, it is clear that as the height of the electrode array is increased, the signal which is observed becomes increasingly blurred.	44
Figure 21. True current density, observed signal, and deconvolved signal at heights of 1 (top), 3 (middle), and 5 (bottom).	45
Figure 22. Mean squared residual of the same signal at heights of 1 (top left), 3 (top right), 5 (bottom left), and 10 (bottom right)	46
Figure 23. Deconvolution from a partial convolved signal with no edge extension (a) edge extension but no windowing (b) and edge extension and windowing (c).	48
Figure 24. Mean squared residual calculations considering the same signal with no extension and no windowing, extension and no windowing, and extension and windowing.....	49

Chapter One: Introduction

Atrial fibrillation (AF) is the most common arrhythmia encountered in clinical practice, having a frequency of 1% in the adult population of North America [1]. Although AF does not cause immediate mortality, it is a potent risk factor for ischemic stroke, accounting for approximately 15% of all strokes in the United States [2, 3]. Further, it has been shown that chronic AF causes structural remodeling of the heart tissue which then increases the chances of AF occurrence [4-6] implicating the need for AF to be treated successfully in a timely manner. A common treatment method for AF is catheter ablation. Here, a catheter is inserted into a patient's venous system, usually entering at the groin, and is guided into the heart. In order to perform an ablation, the tip of the catheter is placed against the heart and radiofrequency electrical current is applied through the catheter. This produces a small burn on the heart muscle, preventing it from being able to conduct current [7]. This procedure has been found to have relatively high overall success rates. Nevertheless, multiple procedures are often necessary in order to completely eliminate the arrhythmia [8].

By mapping the activation patterns of AF prior to ablation the clinician can obtain a view of the electrical activity in a patient's atria. This allows for the creation of individualized ablation plans, which in turn increase the probability of success. Currently, the only option available for mapping prior to an ablation procedure is to use a single roving electrode that maps sequentially throughout the atria. In order for this method to be effective, the activation sequence must not change throughout the mapping period. However, it has been shown that the activation sequence which occurs during AF

is not temporally stable [9], causing sequential mapping to provide an inaccurate representation of the actual activity in the atria. Thus, a new method of mapping is needed in which AF activity is captured simultaneously over an extended region of atrial tissue. For example, an electrode array could be deployed transvenously and used to simultaneously map the activation sequence at multiple locations.

When an electrode is used to map the electrical activity of the atria, what is recorded is not the current density at the recording site. Instead, one obtains a contribution from each current producing site in the tissue weighted inversely by its distance to the electrode. This results in a blurred version of the current density, which can be described as the convolution of the current density field with a point spread function. The point spread function is dependent upon the height of the electrode [10]. This point spread function is convolved with the true current density field to give the observed potential field. Therefore, in principle, deconvolution can be applied to the observed potential field to provide an estimate of the desired current density field. However, practical constraints limit the number of electrodes which can be deployed transvenously, causing the observed potential field to be a sparsely sampled version of the entire field [11]. Furthermore, the electrical potential field inside the atria may not be recorded in its entirety. The truncated edges of a partially sampled potential field cause further problems for deconvolution, and generally require that the edges be windowed or extended in some smooth fashion.

Here, we consider the use of deconvolution to provide an improved estimate of the current density from a sparsely sampled and truncated version of the potential field.

We examine how the density of sampling and a technique for edge extension influence the accuracy of estimates of the current density field.

Chapter Two: Background

2.1 Physiology

2.1.1 Atrial Fibrillation

Atrial fibrillation (AF) is the most common cardiac arrhythmia currently encountered in clinical practice [1] and is projected to have an increasing occurrence among patients in the future as the elderly population continues to grow. AF is associated with increased age, and is thought to occur due to many heart conditions which lead to changes in the atrial myocardium. When AF occurs, the atria undergo a continuous, uncoordinated, rippling type of activity. This activity occurs because the atria do not contract and relax sequentially during each cardiac cycle and therefore do not contribute to ventricular filling [12].

A cardiac arrhythmia occurs when some region of the heart interferes with or alters the normal electrical conduction of the heart [13]. Arrhythmias are often driven by abnormal sources of excitation, which result in circular movement of electrical activity and reentry of conduction [14]. Atrial arrhythmias are known to disrupt the normal sinus rhythm and may arise from an ectopic foci or from the existence of one or more reentrant waves [15]. It is common for AF to be initiated by a premature impulse which arrives during a period in which the excitability of the atrial cells is not uniform. This variation in excitability means some fibers are in the effective refractory state, meaning they are not able to be excited, while others are able to conduct impulses (though at slow conduction velocities). The action potentials are then propagated in multiple wavelets that travel along paths at various conduction velocities. This allows, as cells become

excitable, for reentry of the wave fronts to occur (Figure 1). AF is therefore often self-sustaining, presenting a need for intervention [12, 16].

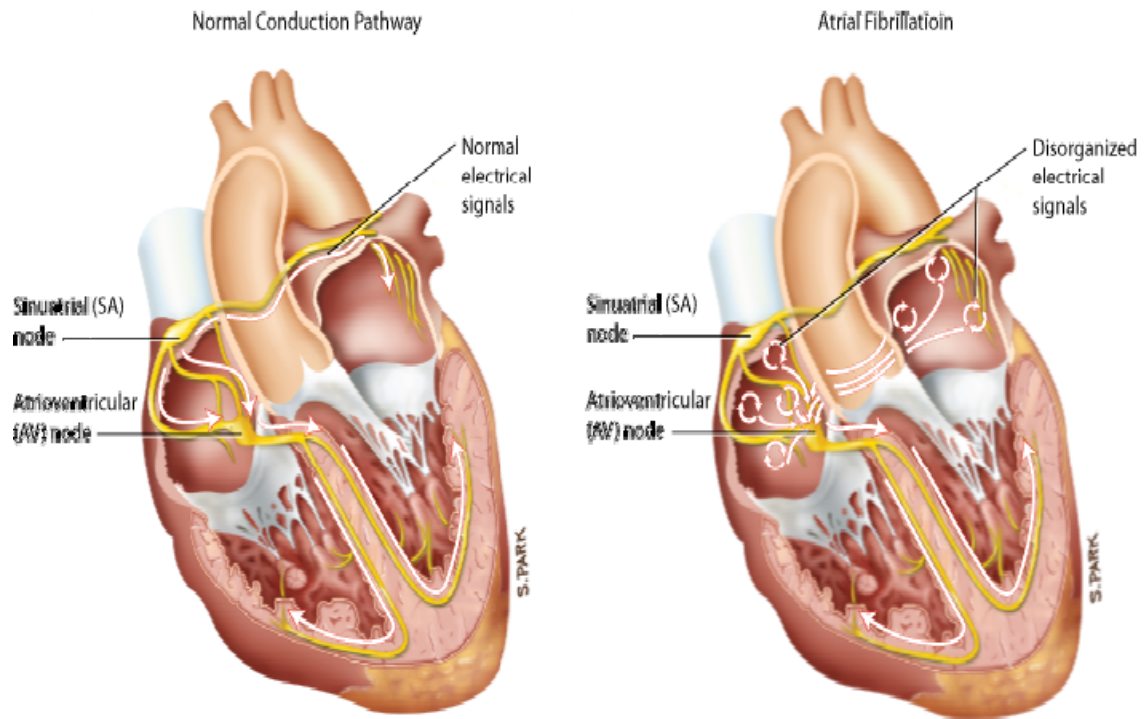


Figure 1. Normal electrical conduction in the heart (left), and disorganized conduction as is seen during atrial fibrillation (right). It is evident that the electrical activity associated with AF exhibits reentry circuits which allow self-sustaining arrhythmic [16].

AF is broken into three categories: paroxysmal, persistent, and permanent.

Paroxysmal AF is intermittent and will self-terminate in less than 7 days. Persistent AF lasts longer but may be terminated by first line pharmacological treatments or electrical cardioversion. Permanent AF implies either that cardioversion has failed or that the patient and physician have decided to allow AF to continue without further efforts to restore sinus rhythm [13, 17, 18]. Although AF does not cause immediate mortality as is associated with its ventricular counterpart, it carries clinical relevance because of its

effects when left untreated [2]. AF is a potent risk factor for ischemic stroke, increasing the risk of stroke 5-fold and accounting for approximately 15% of all strokes in the United States. Although in some patients AF is not symptomatic, for patients with symptoms, AF reduces quality of life, functional status, and cardiac performance and is also associated with higher medical costs and an increased risk of death [3]. Further, it has been shown that chronic AF causes structural remodeling of the heart tissue which then causes AF to be more likely to occur [4-6]. Remodeling occurs due to deposits of connective tissue among atrial myocytes which then lead to electrophysiological heterogeneities. These slow conduction in the atrium and thus lead to the development of reentry circuits [6]. Further, remodeling causes an irregular ventricular response, generally with a higher than average heart rate during sinus rhythm [19]. This occurrence of remodeling implies that the best prevention of AF is to terminate AF as quickly as possible. Further, it has been seen that successful AF treatment and recovery of sinus rhythm can improve and sometimes completely normalize function [6], emphasizing the need for AF to be treated in a successful manner.

2.2 Treatment Methods

2.2.1 Anti-arrhythmic Drug Therapy

Three basic strategies are involved in the treatment of AF: rate control, rhythm control, and therapeutic anticoagulation. In some people, AF causes the formation of blood clots in the atrium which can travel to the brain causing a stroke, and so anticoagulant drugs are often administered daily to prevent clotting [7]. It is known that restoring sinus rhythm is an important factor in treating AF. A variety of data show that

restoring sinus rhythm is better than allowing AF to continue, and further recovery of sinus rhythm can improve and sometimes completely normalize function [2,6]. Although antiarrhythmic drugs have been the core of AF management for a long time, there have been a variety of studies including the AFFIRM and RAFT studies which have shown that the strategy of maintaining sinus rhythm with antiarrhythmics is not better than that of rate control by a β -blocker or calcium-channel blocker in conjunction with anticoagulation [20]. Rhythm control medications are often used to restore sinus rhythm prior to the use of rate control medications in order to manage AF in the long-term [18]. However, it is clear that these medications do not eliminate AF in a large number of patients, causing this method of treatment to likely not be the best choice. Nair states that the efficacy of antiarrhythmic therapy (other than amiodarone) in preventing recurrences at 1 year is around 50% [1]. Such a low efficacy creates the need for other treatment techniques to be used.

2.2.2 Catheter Ablation

Catheter ablation is a second line treatment that has been used for more than a decade to treat drug-refractory AF [21]. The aim of catheter ablation is to eliminate all arrhythmogenic focuses and reentry circuits which may maintain AF [6]. A catheter (a long, thin tube) is inserted into a blood vessel, typically through the groin, and guided through the blood vessels into the heart. The tip of the catheter is then placed against the part of the heart thought to cause the arrhythmia and radiofrequency electrical current is applied through the catheter to produce a small burn [7]. The ideal ablation pattern would prevent AF with a limited number of ablation lines of the shortest possible length,

while allowing for the maintenance of mechanical activity of both atria during sinus rhythm [22]. However, such a pattern for ideal ablation remains unknown. Although ablation technology has improved greatly since the use of ablation therapy began, the mechanism responsible for activation and maintenance of AF remains poorly understood, causing ablation therapy to follow a “one-size-fits-all” approach [21]. In general this involves elimination of all arrhythmogenic focuses in the four pulmonary veins while simultaneously removing the reentry circuits that might trigger and sustain AF. Ablation is also sometimes carried out using linear ablations or focal lesions [6] in an effort to stop reentry circuit conduction (Figure 2). These are general methods and so are not specific to the excitation patterns of a particular patient’s atria.

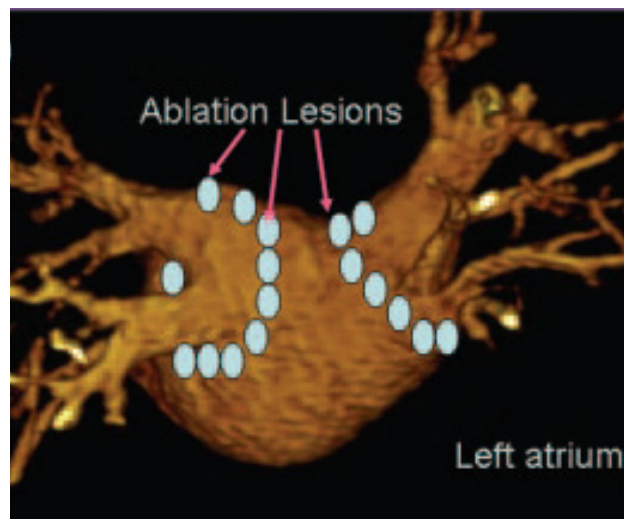


Figure 2. Ablation encircling the pulmonary veins on both sides of the atrium as shown by Ames et al[7]. These lesions are meant to prevent any triggers around the pulmonary veins.

Although there are clear limitations to the use of ablation, it has been noted in multiple studies that AF patients undergoing catheter ablation are less likely to have recurrent AF compared with those treated with anti-arrhythmic medications. Ablation is thus better for long term maintenance of patients [1, 17]. Further, Parkash et al. have

shown that catheter ablation is the best form of rhythm control available for treatment of symptomatic, drug refractory AF. They have also added that the techniques used for catheter ablation should be tailored to the individualized patient [23] emphasizing the importance of mapping the electrical conduction during AF prior to ablation.

2.2.3 Mapping Techniques

Prior to ablation, mapping of the atria can be performed in order to gain an understanding of its electrical activity. Mapping of the electrical excitation of the atria during AF is a powerful technique to gain insight into the fibrillatory process and the related abnormalities in intra-atrial conduction [5]. The term mapping refers to procedures that involve recording local electrical signals at sites of interest and then placing them onto a spatial matrix reflecting the mapping area [24]. Although in research applications mapping can occur with a high resolution, in a clinical setting obtaining high resolution mapping is often not possible. The tools which are used in conjunction with a standard focal mapping catheter result in a relatively low resolution and rely on sequential rather than simultaneous recordings of electrical activity [24-26]. During AF, it is known that excitation patterns are not temporally stable, causing sequential recording to be inaccurate [9]. This then means that the mapped electrical excitation is not precisely that which is occurring at any instant in time.

AF perpetuators are identified by searching for two types of excitation patterns with a roving catheter [20]. Complex Fractionated Atrial Electrogram (CFAE) mapping identifies repetitive low-amplitude high frequency electrograms as ablation targets. CFAE are thought to indicate complex fibrillatory conduction in areas in which the

cardiac tissue structure has been changed. Therefore, CFAE are thought to contribute to the maintenance of AF [27, 28]. Nademanee et al [20] have shown that by ablating areas that have persistent CFAE recordings, AF can be terminated in over 85% of patients. However, it has also been seen in some studies that ablation of CFAE after pulmonary vein isolation did not improve clinical outcomes in patients with long lasting persistent AF [29]. In Dominant Frequency (DF) mapping, focal drivers are identified based upon radially distributed frequency gradients. DF mapping is aimed at identifying localized sites of maximal DF during AF [30]. Sites of high DF should theoretically reflect regions of short cycle length, or drivers, that may be important in maintaining AF [31] and therefore would be important sites for ablation. However, because mapping occurs with a roving catheter, these two procedures are only valid if DF and CFAE remain stable throughout mapping procedure. It has been shown that DF and CFAE do not remain stable throughout the procedure [9] causing this to be an inaccurate representation of atrial excitation.

Although sequential mapping is generally used clinically, it is evident that sequential DF and CFAE maps do not accurately reflect the spatial distribution of excitation frequency during a sampling interval [9]. Therefore, simultaneous recording from multiple sites is necessary in order to allow mapping to be truly useful in AF. Simultaneous mapping can be achieved through the use of an electrode array which allows mapping of an area of cardiac tissue, considering a number of points at once. However, even with the use of simultaneous mapping there is a problem of limited resolution. Due to practical constraints, only a certain number of electrodes can be deployed transvenously, leading to sparse sampling of the electrical potential and

therefore limited sampling resolution. Further, the sampled potential consists of a contribution from every cell in the sheet weighted inversely by the distance of the cell to each electrode [10] causing the observed excitation pattern to be a blurred version of the true signal. To complicate matters further, an array of electrodes can only provide a map of a limited area of the atrial excitation field, causing the observed excitation pattern to be a partial version of the potential field.

2.3 Deconvolution Theory

2.3.1 Convolution and Deconvolution

Often, observed signals are a degraded version of the true signal. This degradation occurs through the process of acquiring the signal which causes the observed signal to be subjected to both noise and blur [32]. When an electrical potential is observed by an electrode placed over the surface of the atria, what is recorded is not the current density at a single site just under the electrode, but instead a signal which consists of the weighted mean of a contribution of the current density in every cell in the tissue. When an observing instrument takes the weighted mean of a physical quantity over a range of some variable, its actions can be described through convolution. The form of the weighting function generally does not change to a significant degree as the central value of the variable changes, which means the observed quantity is a convolved function, rather than the desired quantity itself [33]. In this way, convolution can be used to describe the potential that is recorded using an intra-atrial electrode.

Convolution operates on two functions $g(t)$ and $h(t)$, producing a third function which can be thought of as a modified version of one of the original functions. In this

way it can be thought to “blend” one function with another. Convolution is the integral of the product of two functions, $g(t)$ and $h(t)$, after one of the functions has been shifted and reversed [34,35]. It is given by the equation [33, 36]

$$g(t) * h(t) \equiv \int_{-\infty}^{\infty} g(\tau)h(t - \tau)d\tau \quad (2.1)$$

The electric potential recorded by a sensing electrode can be considered to be the convolution of a point spread function, $(x^2 + y^2 + h^2)^{-1/2}$, with the true current density, $I(z, w, h)$.

Deconvolution is the inverse of convolution and can be used to estimate the true signal. This is generally an ill-conditioned problem as it is extremely sensitive to noise. Further, convolution does not have a simple inverse operation in the time domain. However, by transforming functions into the frequency domain, the inverse can more easily be calculated [37]. Through deconvolution in the frequency domain the true signal, $I(z, w, h)$, can theoretically be obtained if one knows the convolved signal, $\Phi(x, y, h)$, and the blurring signal, $(x^2 + y^2 + h^2)^{-1/2}$.

2.3.2 Fourier Transform

The Fourier transform decomposes a time domain signal into its component frequencies. This provides the frequency domain representation of the signal. By taking the Fourier transform of our signals, deconvolution will now be possible, allowing us to obtain an improved estimate of the current density field. The Fourier transform is given by the equation [36, 37]

$$H(f) = \int_{-\infty}^{\infty} h(t)e^{-2\pi jft} dt \quad (2.2)$$

where $h(t)$ is some time domain signal and $H(f)$ is its Fourier transform.

The convolution theorem allows the Fourier transform of a signal to be used in order to make deconvolution a simple process. The convolution theorem states that convolution in the time domain is equal to multiplication in the frequency domain. This is described by the equation [36, 37]:

$$g(t) * h(t) \Leftrightarrow G(f)H(f) \quad (2.3)$$

where $*$ denotes convolution, $G(f)$ is the Fourier transform of $g(t)$ and $H(f)$ is the Fourier transform of $h(t)$. The convolution theorem can be derived as follows:

Convolution of $g(t)$ with $h(t)$ is defined as:

$$\int_{-\infty}^{\infty} g(\tau)h(t - \tau)d\tau$$

The Fourier transform of this convolution is equal to:

$$\begin{aligned} & \int_{-\infty}^{\infty} \left[\int_{-\infty}^{\infty} g(\tau)h(t - \tau)d\tau \right] e^{-2\pi jft} dt \\ &= \int_{-\infty}^{\infty} g(\tau) \left[\int_{-\infty}^{\infty} h(t - \tau)e^{-2\pi jft} dt \right] d\tau \end{aligned}$$

By the definition of the Fourier transform, this is equal to [33]:

$$\begin{aligned} &= \int_{-\infty}^{\infty} g(\tau)e^{-2\pi jft} H(f)d\tau \\ &= G(f)H(f) \end{aligned}$$

Because of this, if we have a convolved signal, in the frequency domain it can be described as $Y(f) = X(f)H(f)$. Further, to deconvolve this signal in order to solve for

$X(f)$ we can simply divide the convolved signal by the signal with which $X(f)$ was convolved, i.e. $X(f) = \frac{Y(f)}{H(f)}$. The inverse Fourier transform of $X(f)$ would therefore be

equal to $x(t)$ which has been shown to be equal to the inverse Fourier transform of $\frac{Y(f)}{H(f)}$.

In the current problem, the electric potential field, $\Phi(x, y, h)$, which is observed, consists of the true tissue current density field, $I(z, w, h)$, convolved with $(x^2 + y^2 + h^2)^{-1/2}$, the point spread function that reflects the contribution of every cell in the tissue. This is described by the equation:

$$\Phi(x, y, h) = I(z, w, h) * (x^2 + y^2 + h^2)^{-1/2}$$

Due to the convolution theorem described above, it can be seen

$$\mathfrak{F}\{\Phi(x, y, h)\} = \mathfrak{F}\{I(z, w, h)\} \cdot \mathfrak{F}\{(x^2 + y^2 + h^2)^{-1/2}\}.$$

Where $\mathfrak{F}\{ \}$ denotes the Fourier transform of the bracketed quantity. Therefore,

$$\mathfrak{F}\{I(z, w, h)\} = \frac{\mathfrak{F}\{\Phi(x, y, h)\}}{\mathfrak{F}\{(x^2 + y^2 + h^2)^{-1/2}\}}.$$

This then means that the inverse Fourier transform of the Fourier transform of $I(z, w, h)$ is equal to the inverse Fourier transform of this quotient:

$$\mathfrak{F}^{-1}[\mathfrak{F}\{I(z, w, h)\}] = \mathfrak{F}^{-1}\left(\frac{\mathfrak{F}\{\Phi(x, y, h)\}}{\mathfrak{F}\{(x^2 + y^2 + h^2)^{-1/2}\}}\right).$$

In other words, $I(z, w, h)$ is equal to:

$$I(z, w, h) = \mathfrak{F}^{-1}\left(\frac{\mathfrak{F}\{\Phi(x, y, h)\}}{\mathfrak{F}\{(x^2 + y^2 + h^2)^{-1/2}\}}\right).$$

2.3.3 Effects of Noise

This process of deconvolution proves extremely sensitive to noise which may be present in the data. One reason for such a problem occurs when the use of Fourier transforms to perform deconvolution results in division by zero [36]. In our study, this occurs when numerical errors cause the Fourier transform of the recorded potential to hold a significant value while the point spread function is equal to, or very close to, zero.

When deconvolution is used as described above, this will result in large oscillatory artifacts being created in the estimate of the true signal, leading to a result that will not prove useful. In order to overcome this problem, the theory of the Wiener filter is invoked. This theory involves adding a small delta function to the center of the point spread function, which has the effect of adding a small constant to the transform of the point spread function [38]. Our estimate of the true current density is now described as

$$I(z, y, h) = \mathfrak{F}^{-1} \left\{ \frac{\mathfrak{F}\{\Phi(x, y, h)\}}{\mathfrak{F}\{I(x^2 + y^2 + h^2)\} + c} \right\}.$$

2.3.4 Data Truncation

The extent of the electrical potential field which is recorded within the heart is always limited, providing us with a truncated potential field. Having a partial version of the potential field has an important effect upon our ability to use deconvolution. Sensing a partial version of the potential field can be described by multiplying a rectangular window of height 1 by the observed field. Because multiplication in the time domain is equivalent to convolution in the frequency domain, when we take the Fourier transform of the observed potential field it has the effect of convolving the transform of the entire

potential field with the transform of the rectangular window, which is a sinc function ($\text{sinc}(x) = \frac{\sin(x)}{x}$). This then will result in spectral leakage, causing significant distortion of the deconvolved signal [39, 40]. In order to avoid this, edge extension or windowing can be applied to the data to smoothly extend its edges to zero prior to taking the Fourier transform. This will reduce the effects created by deconvolving a partial version of the potential field and provide a more accurate depiction of the desired signal, here the current density field.

2.4 Simulation of Atrial Activation

Because mapping of atrial activation is restricted by sampling limitations, the nature of AF in a given patient often remains unknown. This makes it difficult to determine the relationship between the patterns of electrical excitation in the heart and the electrogram which is recorded. On the other hand, computer models can be used to precisely relate a simulated excitation pattern to the observed electrogram [41]. A variety of computer models have been created which simulate activation patterns in the atria in an attempt to accomplish this goal. These models exhibit various features which are meant to replicate the environment of the atria in order to create realistic activation patterns. Due to the limitations of computer processing speeds, however, a compromise must be reached between the simulation speed, complexity of the cellular membrane model, complexity of the tissue, the number of spatial nodes, complexity of the anatomy, the duration of the simulated events, and the accuracy of the methods used [42]. This has led to the creation of many biophysical models of the human atria which consider the tradeoff between computation speed and anatomical representation in different ways [22].

A variety of models have been created which consider a 3-D model of the atria to allow for the effects of geometry which are implicated in the activation patterns seen in arrhythmias (Figure 3). Many of these models further increase complexity and include cellular ionic models. However, the computational overhead in these models causes them to run much slower than real time, often taking multiple hours to process seconds of activation [15, 42]. Other models consider a more simplified view of the geometry, looking at the atria in 2-D and therefore allowing for greater speeds in simulation. These models often attempt to preserve realistic tissue properties while adding speed through the use of a simpler geometry [28].

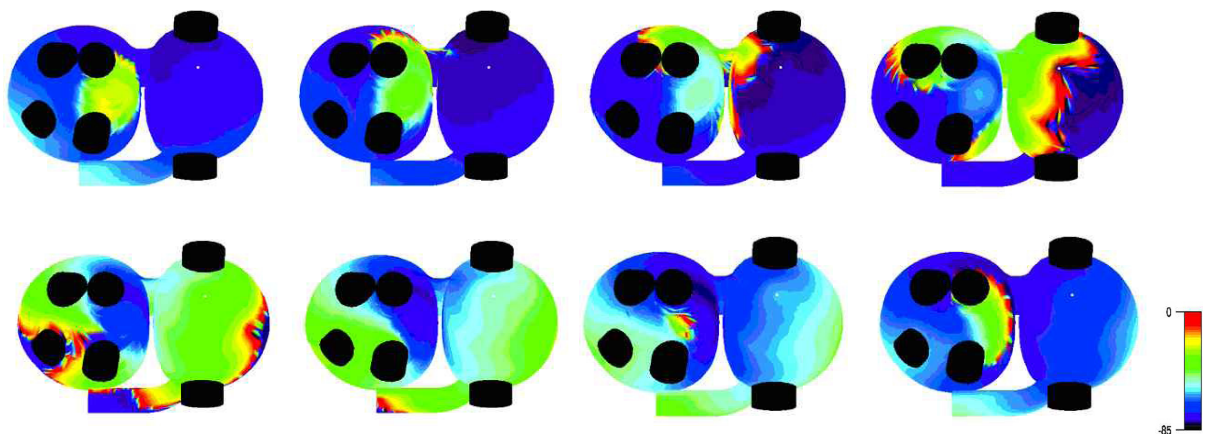


Figure 3. Reentry shown in a physiologically realistic model as is seen in the model created by Vigmond et al [15]. This model can be seen to have realistic anatomical properties at the expense of a slow running time.

Even simpler models, which allow for an even greater speed, are based on cellular automata. These models allow for cells to be in distinct states (excited, refractory or quiescent), to be built in a simple structure, and to follow a simplified set of rules which govern the way in which the cells act as a function of their interaction with their neighbors [43]. Various cellular automaton models of cardiac tissue have been created.

Such models may include parameters such as a refractory state, allowing for complex propagation patterns to be simulated [44, 45].

The model used here is a cellular automaton model in which the cells have a voltage that varies with time. Each cell is electrically connected to its neighbors with which it exchanges current according to Ohm law. This means that the cell voltage is altered both through extra-cellular current flow during activation and through exchange of current with each of its neighbors [43]. This model was used to simulate activation patterns typical of AF in order to create a known current density map (Figure 4) which could be sampled by specified electrode arrays and used in order to study the improvements that can be made through deconvolution.

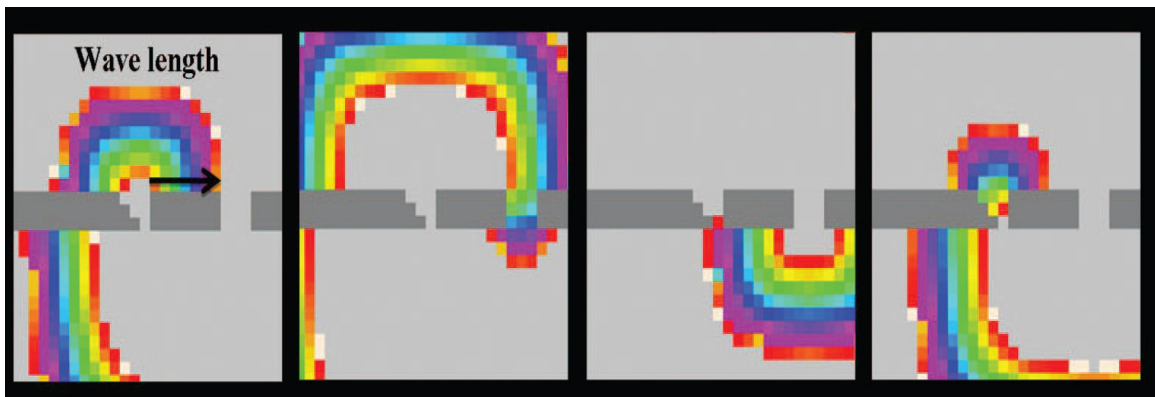


Figure 4. Reentry secondary to fixed, anatomic substrate, as seen in the model by Spector et al [43]. This cellular automaton model was used to create current density fields to be used in this study.

Chapter Three: Deconvolution in One Dimension

3.1 Background

The electrical potential recorded by an array of electrodes above atrial tissue can be described as the current density field of the tissue convolved with a point spread function as described in section 2.3.1. If the observed potential consists of a complete convolved signal, it can be improved through deconvolution using Fourier transforms as explained in section 2.3.2. However, the signal obtained through the use of an array of intra-atrial electrodes is not the complete convolved signal but rather is limited by sampling constraints related to the number of electrodes that can be deployed transvenously. The limited number of sensing electrodes causes sparse sampling of the electrical potential. The apparent potential map is therefore a coarsely sampled portion of the true potential field. The success of deconvolution in improving the signal resolution therefore depends upon the number of electrodes in the sampling array. Consequently, it is necessary to determine the size of the electrode array required in order to provide an improved signal using deconvolution. Here we look specifically at the minimum number of sensing electrodes which are necessary to improve the resolution of the observed signal using deconvolution at various electrode heights.

3.2 Computational Methods

We consider the electric potential which would be recorded by intra-atrial electrodes during a mapping procedure. The signal considered corresponds to any instant in time, and is therefore snapshot of the electric potential produced by atrial fibrillation. We consider the atrial tissue to be two-dimensional. Such a situation would occur if one

was mapping over a region of tissue of uniform thickness which was small enough in extent to be essentially a flat plane. Further, in order to simplify this situation, we look at the problem in one dimension.

A one dimensional signal is blurred through convolution as occurs when an electrode is used to determine the electric potential. The original signal (the signal which is given before convolution occurs), will then be used as the current density field, the “true signal” which we desire (Figure 5). This means that the signal which we are trying to determine is known, allowing for a comparison between our result and the true signal. Here each unit in the x direction is a unit of location and can be considered to be 1 mm, units in the y direction represent the quantity of current which is observed.

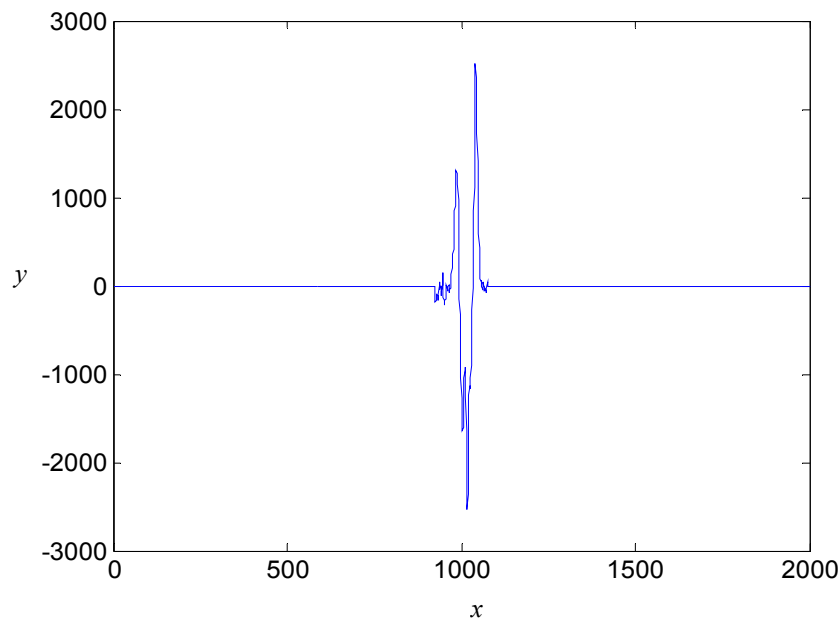


Figure 5. Example of the current density - $I(x, y)$.

When an electrode is placed at height, h , above the tissue, the electric potential, Φ , which is recorded consists of a contribution from every cell in the sheet weighted

inversely by the linear distance from the cell to the electrode. In one dimension this is described by the equation:

$$\Phi(x, h) = \int_{-\infty}^{\infty} \frac{I(x, y)}{\sqrt{(x-z)^2 + h^2}} dz \quad (3.1)$$

Due to the definition of convolution, equation 3.1 is equal to [10]

$$\Phi(x, h) = I(x, y) * \frac{1}{\sqrt{(x-z)^2 + h^2}} \quad (3.2)$$

(where * denotes convolution). Therefore, the measured signal is a blurred version of the true signal, as can be seen in

Figure 6. Because both the convolved signal as well as the point spread function with which the true signal is convolved are known, in principle, $I(x, y)$ can be found using deconvolution.

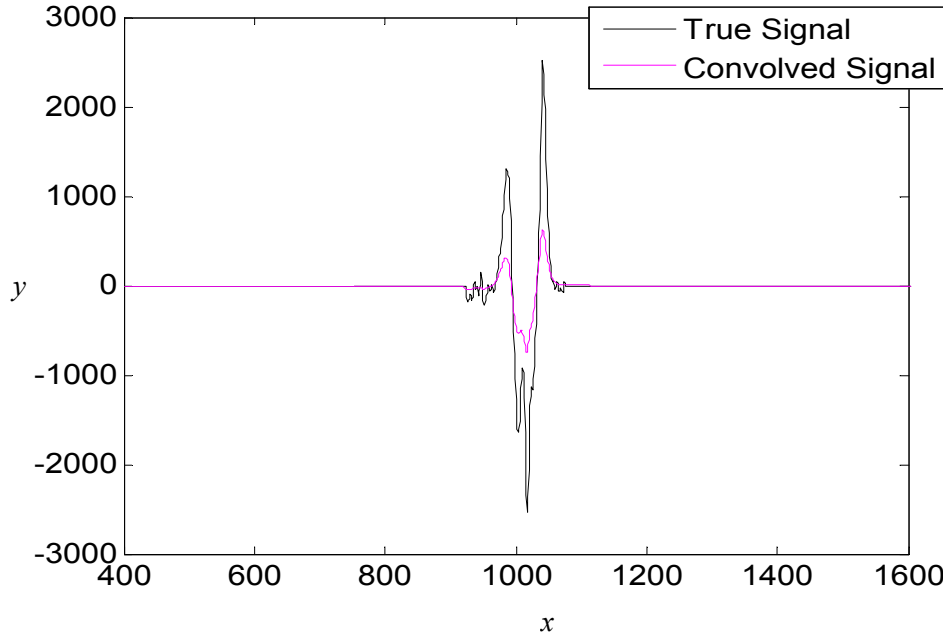


Figure 6. Example of the convolved signal, $\Phi(x)$, which consists of the current density convolved with the point spread function.

However, the signal is recorded by a limited number of sensing electrodes, providing a sparsely sampled potential. Because of this, interpolation of $\Phi(x)$ between the electrode sites is necessary before Fourier deconvolution can be attempted. Here, cubic spline interpolation was used in order to provide an estimate of the potential field, $\Phi(x)$ (

Figure 7). Further, due to limitations of the area of the tissue which can be covered by an array of electrodes, the recorded signal is generally not the complete signal but instead is a partial version of it. This causes significant oscillatory effects when Fourier deconvolution is used. Therefore, if a partial version of the potential field is obtained the truncated edges of the signal must be smoothly extended to zero before Fourier deconvolution can be used, as explained in section 2.3.2.

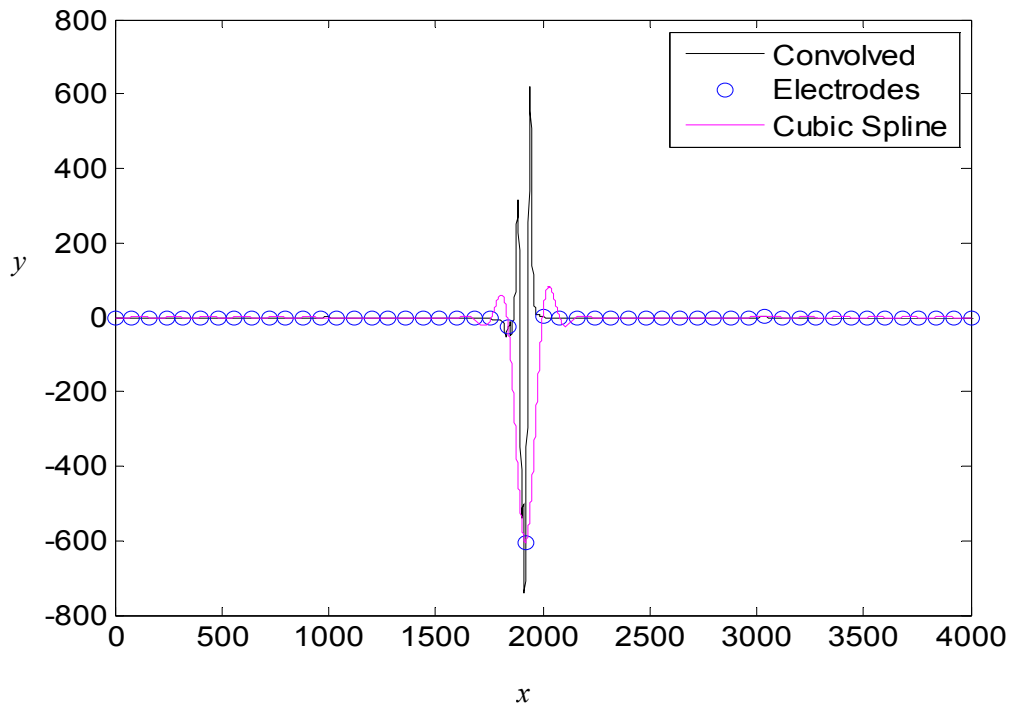


Figure 7. Example of the cubic spline interpolation (shown in pink) found using 50 electrodes to sample the convolved signal.

In principle, an estimation of the true signal can be found from $\Phi(x)$ by division by the point spread function in the Fourier domain. However, inevitable numerical errors cause the transform of the point spread function to be zero, or very close to zero, at frequencies for which the Fourier transform of $\Phi(x)$ has a significant value. We therefore invoke the theory of the Wiener filter by adding a small delta function to the center of the point spread function. This has the effect of adding a small constant ($c = .5$) to the transform of the point spread function [38]. An estimate of the true signal is thus found to be

$$\hat{I}(x, y) = \mathfrak{F}^{-1} \left\{ \frac{\Phi(u, h)}{f(u, h) + c} \right\} \quad (3.3)$$

Where $\mathfrak{F}^{-1} \{ \}$ denotes the inverse Fourier transform of the bracketed quantity and $\Phi(u, h)$ and $f(u, h)$ are the 1-D Fourier transforms of $\Phi(x)$ and the point-spread function respectively.

In order to determine the impact of the number of sensing electrodes on the deconvolved signal, the consequence of varying electrode array size was tested at specified electrode heights. This was used to provide an indication of how small the number of sensing electrodes can be while continuing to provide improvement using deconvolution. The mean squared residual (MSR) of both the observed and deconvolved signals relative to the true signal were used to quantify this result. The mean squared residual is calculated by dividing the sum of squared residuals by the number of parameters, m , subtracted from the number of measurements, n . That is

$$MSR_{obs} = \frac{SSR}{n-m} = \frac{\sum_{i=1}^n (I_i - \Phi_i)^2}{n-m}$$

$$MSR_{dec} = \frac{SSR}{n-m} = \frac{\sum_{i=1}^n (I_i - \hat{I}_i)^2}{n-m} \quad (3.4)$$

where I is the value of the true signal, Φ is the potential found through equation 3.2, and \hat{I} is the deconvolved signal predicted by equation 3.3 [46]. In order to determine the influence of electrode height, MSR_{obs} and MSR_{dec} were determined for a range of values of h in equation 3.2.

3.3 Results

3.3.1 Effects of Electrode Array Size

Figure 8 shows the true current density, observed electric potential and deconvolved signal found using an electrode spacing of 4 (a) and 40 (b). Deconvolution is able to improve the resolution of the measured signal, causing it to be more like the true signal if there are a sufficient number of sensing electrodes. Using a dense electrode array, the deconvolved signal is a nearly perfect estimate of the true current density (a). However, if there is a large spacing between electrodes this is not as effective (b). The deconvolved signal can thus be seen to be less similar to the true current density when using a greater spacing than with the dense electrode array.

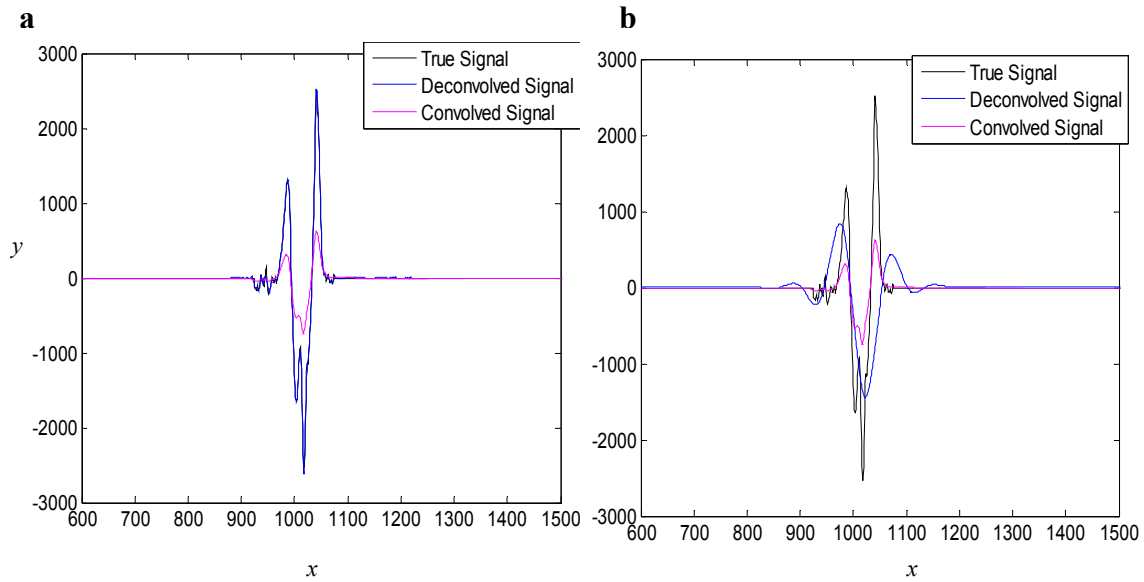


Figure 8. Images showing the deconvolved signal (blue) the convolved signal (pink) and the true signal (black) at electrode spacing of 4 (a) and 40 (b). It is clear that the deconvolved signal provides more closely resembles the true signal when compared to the convolved signal.

Figure 9 shows MSR_{obs} and MSR_{dec} as the number of sensing electrodes is increased at electrode heights of 25 (a) and 150 (b). At both heights MSR_{dec} is smaller than MSR_{obs} indicating that the deconvolved signal is more similar to the true current density than the observed signal. Further, as the number of electrodes is increased, MSR_{dec} continues to decrease, indicating a greater improvement in resolution. With a small number of electrodes resolution improvement is not significant and approximately 15 electrodes are needed in order to provide a significant improvement through deconvolution. At a height of 25 (a) the improvement is greater than the improvements at a height of 150 (b).

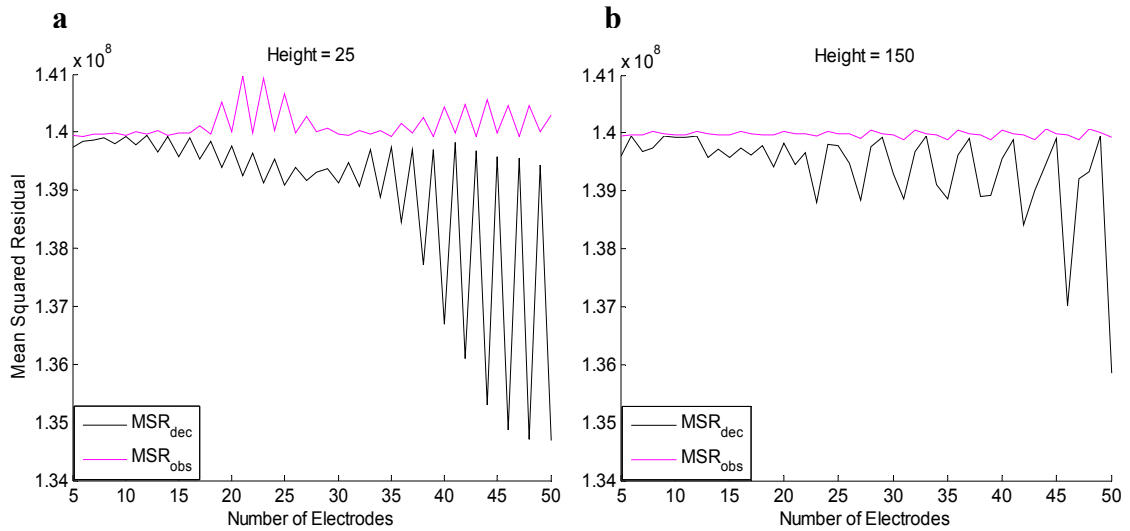


Figure 9. Mean squared residual values of the deconvolved and observed signals varying electrode spacing with electrode height of 25 (a) and 150 (b). It can be seen that as the number of electrodes increases, deconvolution provides greater improvement when compared to the observed signal.

The graphs in Figure 9 show a jagged behavior of increasing and decreasing improvement in both MSR_{obs} and MSR_{dec} . This behavior is due to the location of the placement of electrodes when observing the electric potential. Figure 10 shows MSR_{dec} with the electrodes in their original location and with the placement of electrodes shifted by 1 prior to deconvolution. If the electrodes are shifted, this oscillatory effect is also shifted and changed. This indicates that the behavior observed is due to the placement of electrodes along the current density field.

3.3.2 Effects of Electrode Height

Figure 11 shows MSR_{obs} as electrode height is increased. An increase in the MSR_{obs} value occurs sharply until it reaches an asymptotic value at an electrode height of about 50 at which point the increasing of electrode height has little effect on the observed signal.

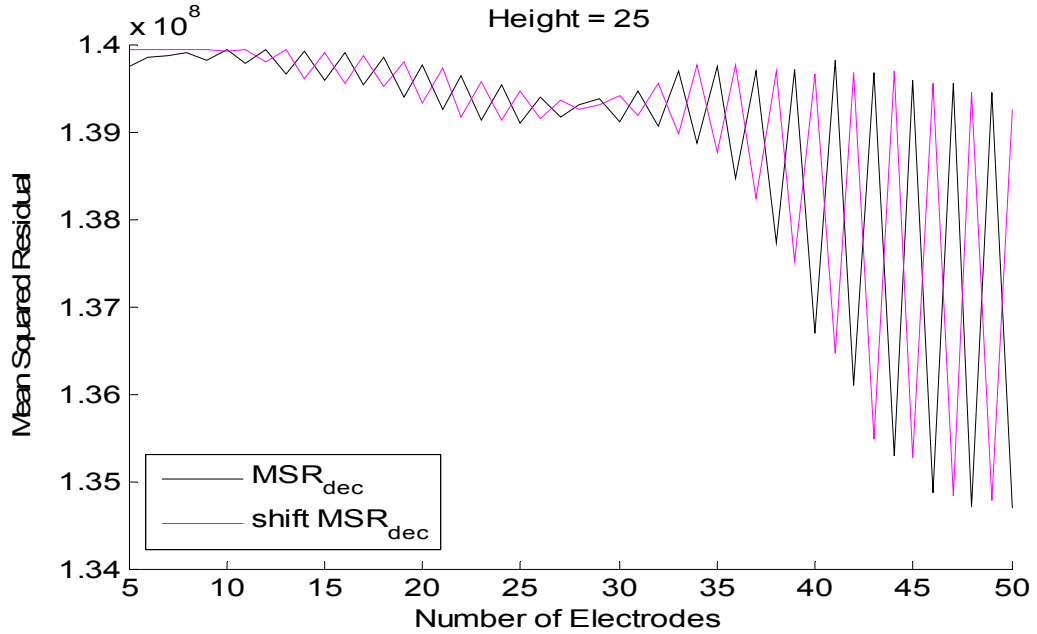


Figure 10. MSR calculated when the electrode location is shifted by 1. It is clear that this shift in electrode locations shifts the oscillatory effects.

Figure 9 shows both MSR_{obs} and MSR_{dec} at electrode heights of 25 and 150 and demonstrates that the improvements which can be made are effected by the height of the sensing electrode. If the electrode height is greater, deconvolution provides a more considerable improvement with a smaller number of electrodes. In order to cause significant improvement at a height of 25 approximately 16 electrodes are needed while with a height of 150 only about 13 electrodes are needed. However, after reaching this threshold number of electrodes, the improvements are uniformly greater when considering using a lower electrode height.

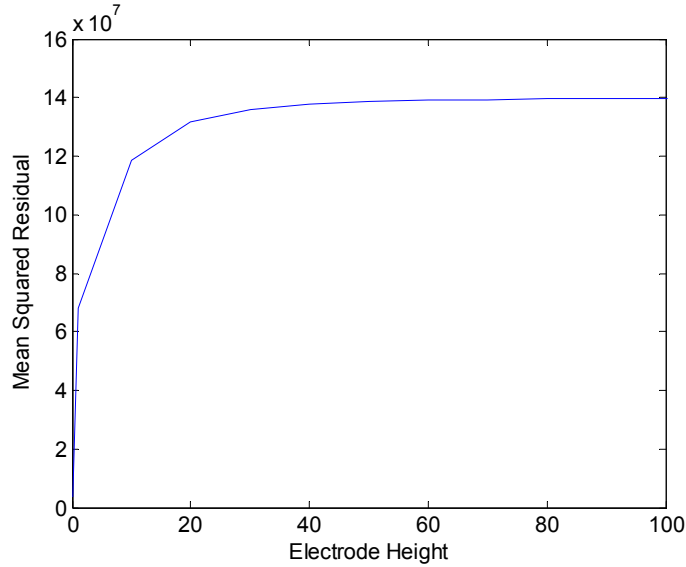


Figure 11. The mean squared residual value calculated between the "true signal" and the convolved signal becomes increasingly large as the electrode height is increased.

3.4 Discussion

The results of this initial test of the utility of deconvolution indicate that deconvolution is useful in providing an improved estimate of the true current density from the observed potential. Figure 8 clearly demonstrates that with a high density of electrodes, as can be seen in the left image (a), deconvolution provides a signal which much more closely resembles the true current density than the signal which is observed. However, as can be seen in the right image (b) which shows a much larger electrode spacing, the improvement is less clear when spacing between sensing electrodes is large. Calculation of MSR_{obs} and MSR_{dec} , shown in Figure 9, indicate that as the number of electrodes increases improvement due to deconvolution becomes increasingly significant. Deconvolution is able to provide improvement upon the observed signal with any electrode array. However, this improvement is not significant with very small arrays and

about 15 electrodes are necessary in order to make significant improvements. The values of MSR_{obs} and MSR_{dec} seen in Figure 9 follow a jagged pattern with an oscillation of improvement as the number of electrodes increases. Figure 10 demonstrates that this behavior changes when the location of the sensing electrodes is shifted. This indicates that this oscillatory pattern is due to the location of the sensing electrodes. It is likely this is due to the placement of electrodes missing parts of the true current density and therefore limiting the improvements which can be made through deconvolution. Electrode location may prove to be an important factor in application of this method of deconvolution. It would likely be important to consider shifting the electrodes slightly throughout recording to ensure recording of as much of the potential field as possible and therefore obtain the greatest results.

Comparison of the two images in Figure 9 also demonstrates that electrode height influences the improvements which can be made through deconvolution. It is clear that with the greater height, seen on the right, deconvolution is able to more quickly provide a clearly improved estimation of the true signal; however, at a lower height, once the threshold number of electrodes is reached, the improvement due to deconvolution is more significant. Further, as is shown in Figure 11, as electrode height is increased, the observed signal becomes increasingly blurred and more unlike the true current density. Therefore, although improvements are significant at a greater height, they are not necessarily the most useful. It is best instead to use a lower sensing height with a slightly larger number of sensing electrodes to achieve the greatest improvement.

This initial test of deconvolution clearly indicates that when we consider a simple one dimensional signal at one instant in time, deconvolution proves useful with

approximately 15 electrodes. Although here we use a clearly simplified current density, it provides an indication that deconvolution is a useful tool in order to improve our estimate of the current density found in atrial tissue. This problem has been previously considered using a polynomial method of deconvolution in one dimension. It was found that this method of deconvolution could provide an improved estimate of the true signal.

However, the improvement made was highly dependent upon the number of electrodes as the solution to this problem using a polynomial method is not unique [10]. The results of our study are also dependent upon the number of electrodes used; however, here it was found that an improvement can be made even with a small number of sensing electrodes but that this improvement was not greatly significant. Such a result implies that this method of deconvolution provides an improved ability to estimate the true current density.

The improvement which is evident with our result is further confirmed by the work of Chouvarda et al [11] which considered using similar deconvolution methods for membrane current estimation in simulated infarcted myocardium. This study found that in two dimensions, using a somewhat sparse number of sensing electrodes, deconvolution is able to provide an improved estimate of the membrane current. Their result adds to our evidence that our use of deconvolution can prove a useful tool. This then indicates that it is worthwhile to consider this process in two dimensions in order to improve our understanding of the utility of deconvolution with more realistic current density fields.

Chapter Four: Deconvolution in Two Dimensions

4.1 Background

As we have seen in the previous chapters, the signal which is recorded by an array of electrodes placed at a certain height above atrial tissue can be described by the convolution of the current density field with a point spread function. Because of this, if we were to obtain the complete convolved signal, deconvolution using Fourier transforms could be used to obtain the true current density from the observed potential field. However, as was seen when considering a one dimensional electric potential, the signal obtained through the use of intra-atrial electrodes is not the complete convolved signal.

Here we extend the work of the previous chapter to consider a two dimensional current density field. We apply deconvolution to a current density field simulated by a computational model of atrial excitation. As before, we examine the effects of the number of electrodes in the array used to record the potential map as well as the effects of map truncation. In particular, we consider the use of an edge extension technique to bring the truncated edges of the sampled field smoothly down to zero.

4.2 Computational Methods

As was seen when using deconvolution in one dimension, we consider the signal at snapshots in time of the electric potential which would be recorded by intra-atrial electrodes during a mapping procedure. We consider the tissue to be two-dimensional, as would occur if one was mapping over a small flat region of tissue of uniform thickness. Here we consider each cell in our sheet of tissue to represent a 1 x 1 mm square of tissue. The height of our sensing electrodes is then based upon the units of the tissue, each unit

of height is then considered to represent 1 mm. As explained above, the electric potential recorded is not the true current density, but instead is influenced by every cell in the tissue. The electric potential, Φ , recorded by the electrode at a height, h , above the tissue, consists of a contribution from every cell in the sheet weighted inversely by the linear distance from the cell to the electrode:

$$\Phi(x, y, h) = \int_{-\infty}^{\infty} \int_{-\infty}^{\infty} \frac{I(z, w, h)}{\sqrt{(x-z)^2 + (y-w)^2 + h^2}} dzdw \quad (4.1)$$

where $I(z, w, h)$ is the current density and $\frac{1}{\sqrt{(x-z)^2 + (y-w)^2 + h^2}}$ is the point spread function [10]. Equation 4.1 can be described as

$$\Phi(x, y, h) = I(z, w, h) * \frac{1}{\sqrt{(x-z)^2 + (y-w)^2 + h^2}}. \quad (4.2)$$

(where * denotes convolution).

Here a two dimensional signal is blurred through convolution using equation 4.2 in order to simulate an observed potential field, $\Phi(x, y, h)$, which would be recorded by an array of electrodes. The original signal is then the current density field which we are trying to estimate (Figure 12). The point spread function which is convolved with our true current density can be calculated as described above. This means that if the entire extent of the convolved signal was known, deconvolution could be used in order to estimate $I(z, w, h)$ from $\Phi(x, y, h)$.

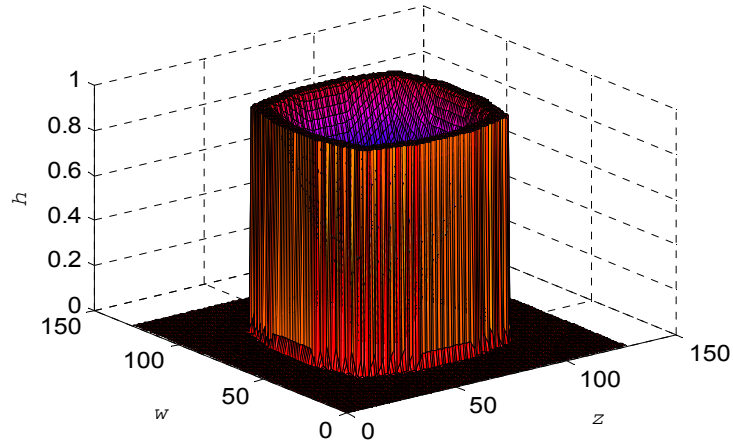


Figure 12. Example of the true current density field $I(z,w,h)$.

However, as was seen in one dimension, the observed signal is recorded using a specific number of electrodes whose spacing may not be uniform and is generally sparse. We therefore sample the potential field only at a specified number of points. Because the extracellular potential field is actually continuous, we interpolate between the electrode locations in order to create a continuous signal from the electrode recordings. Here we use cubic spline interpolation in order to accomplish this task (Figure 13).

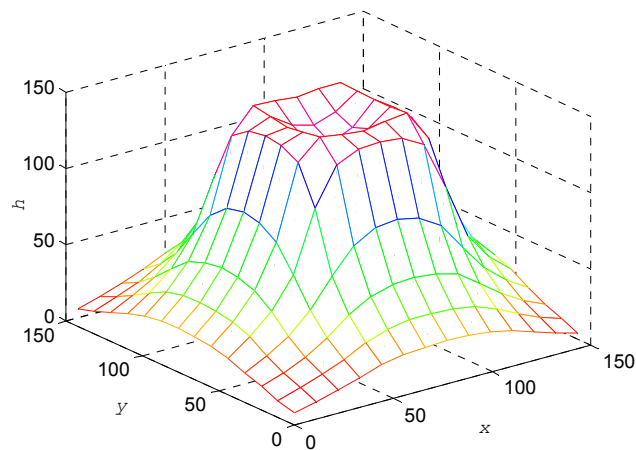


Figure 13. Example of an interpolated convolved signal with an electrode spacing of 15. Cubic spline interpolation occurs between the electrodes prior to Fourier deconvolution.

Further, what is recorded is usually a truncated version of the potential field, as the electrode array will not cover the entire extent of the atrial tissue. Therefore, the effect of recording a partial signal on Fourier deconvolution must also be considered. The recording of a partial signal means the edges of the potential field are truncated, leading to oscillatory effects in the deconvolved signal. To avoid such edge effects, the signal is extended in all directions by half the width of the point spread function using point-wise first derivative matching of the edges of the observed signal. This extended signal is then multiplied by a unique window consisting of a cosine bell that extends half of the length of the point spread function in each direction, surrounding a square of height 1. The width of the square is equal to that of the observed potential field minus half the width of the point spread function (Figure 14).

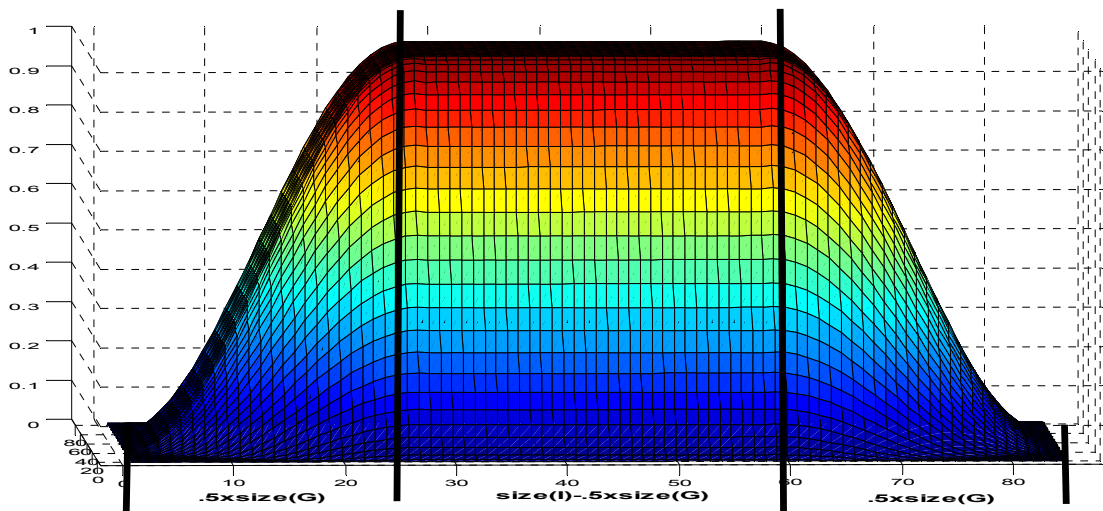


Figure 14. The window used to smoothly extend the convolved signal. The window consists of a square which is equal to half the size of the point spread function (G) subtracted from the size of the convolved signal (I), this square is surrounded by a cosine bell which extends half the size of the point spread function (G) in each direction.

This technique allows the signal to extend smoothly to zero without losing a large portion of the initial data, most of which falls under the square area of the window of

height 1 and therefore keeps its initial value (Figure 15). Multiplication of the extended signal with the window provides an estimate of the observed signal, $\tilde{\Phi}(x, y, h)$, upon which signal resolution improvement can be used. Deconvolution using the Fourier transforms of $\tilde{\Phi}(x, y, h)$ and the point spread function can now occur as explained in section 2.3.2.

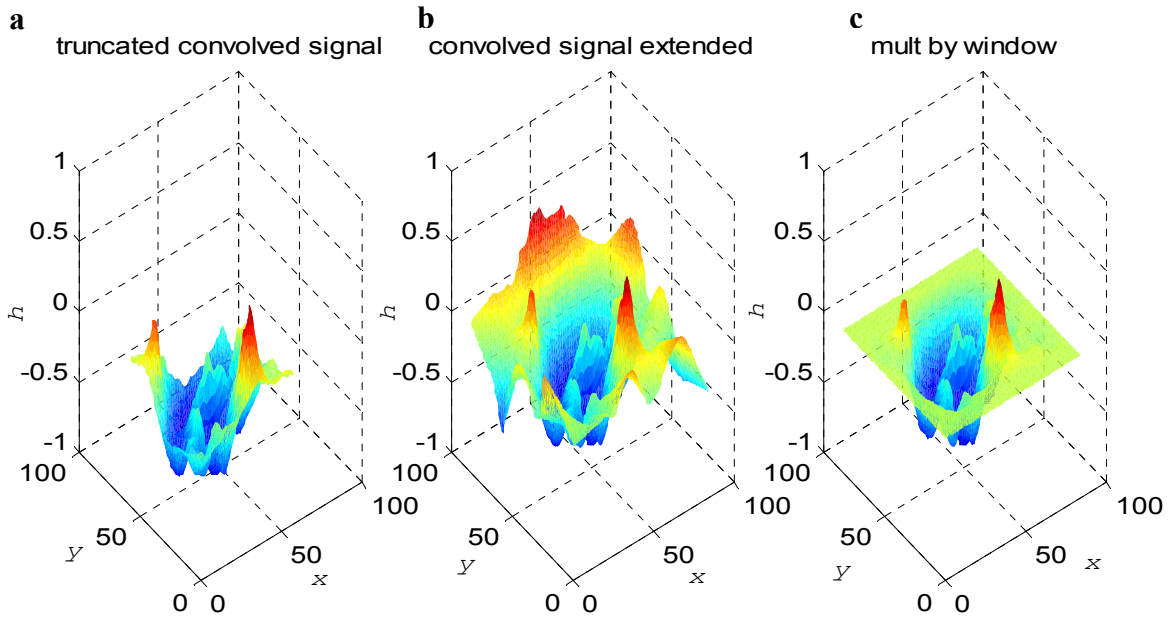


Figure 15. Example of a truncated convolved signal (a), smooth edge extension applied to the signal (b), and the extended signal multiplied by our window (c). It can be seen that the use of edge extension allows the signal to smoothly extend to zero and avoid edge effects when the Fourier transform is used to perform deconvolution.

Theoretically the true signal can be found from $\tilde{\Phi}(x, y, h)$ simply by division in the Fourier domain, however, as was seen in one dimension, the transform of the point spread function is often zero at spatial frequencies for which the Fourier transform of $\tilde{\Phi}(x, y, h)$ has significant power. This results in large oscillatory artifacts in estimates of the current density. Therefore, we again invoke the theory of the Wiener filter by adding a small delta function to the point spread function, which has the effect of adding a small

constant to the transform of the point spread function [38]. This provides an estimate of $I(x, y)$ as

$$\hat{I}(x, y) = \mathfrak{F}^{-1} \left\{ \frac{\Phi(u, v, h)}{f(u, v, h) + c} \right\} \quad (4.3)$$

where $\mathfrak{F}^{-1} \{ \}$ denotes the inverse Fourier transform of the bracketed quantity and $\Phi(u, v, h)$ and $f(u, v, h)$ are the 2-D Fourier transforms of $\tilde{\Phi}(x, y, h)$ and the point-spread function respectively.

In order to determine the effect of electrode array size, at specific electrode heights, the impact of varying electrode spacing on both the observed and deconvolved signals was tested. This was used to indicate how small of an electrode array can be used while deconvolution continues to provide an improved signal when compared to that which would be observed. This result of varying the electrode array size was quantified through calculation of MSR_{obs} and MSR_{dec} using equation 3.4. Comparison of these values allows for a clear indication of the improvement deconvolution has upon the observed signal.

The influence of electrode height upon the utility of deconvolution was also considered. At specified electrode array sizes, the height of the electrode array was varied. The impact of these variations on both the observed and deconvolved signal was considered. MSR_{obs} and MSR_{dec} were again calculated to provide a clear indication about the impact of electrode height on the utility of deconvolution.

Further, we considered the impact of the use of edge extension and windowing upon the observed signal prior to the use of deconvolution. Using specified electrode array sizes and heights, we compared the utility of deconvolution on the observed signal

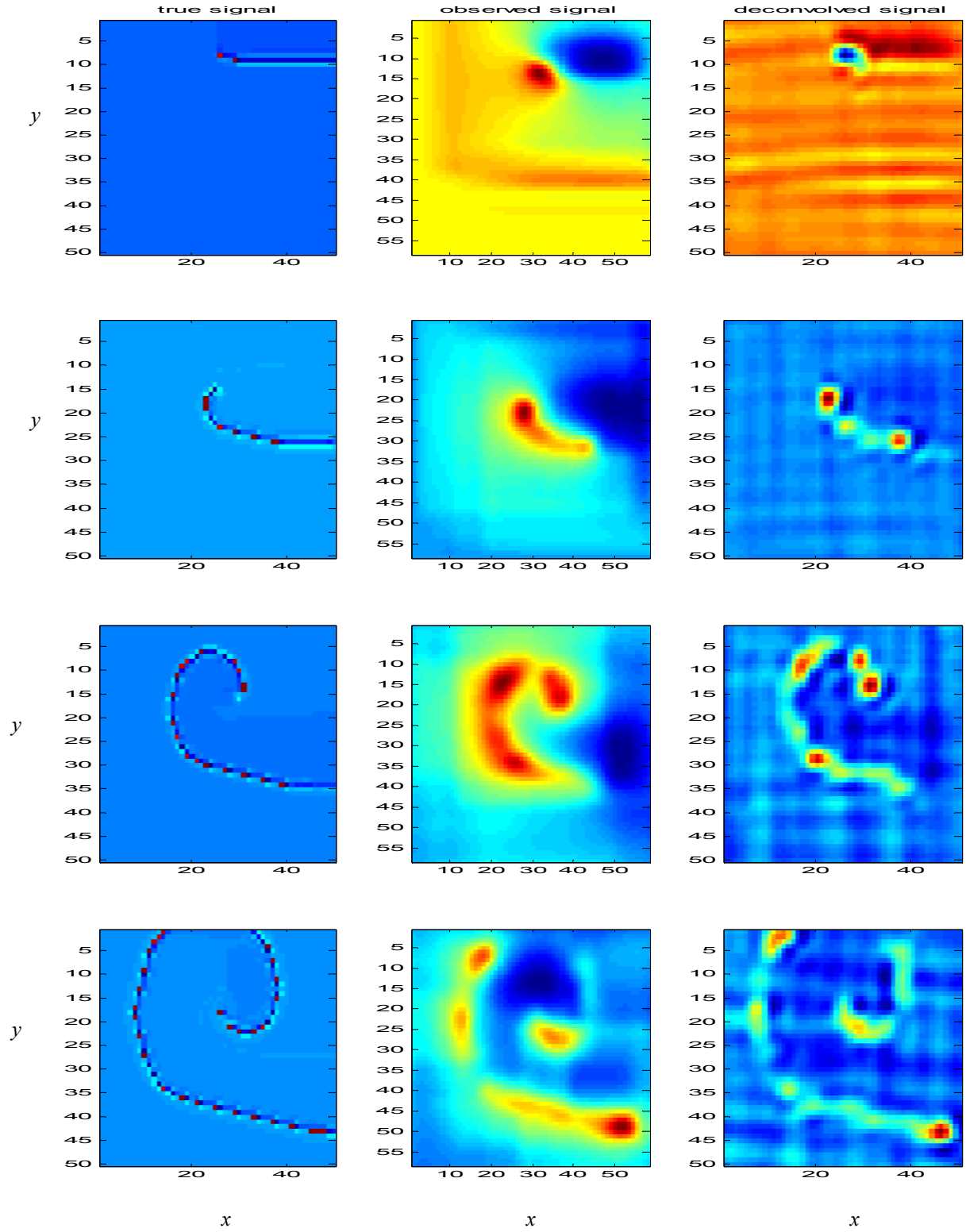
prior to the use of edge extension and windowing to the utility of deconvolution after these techniques have been used. The comparison of these signals was used to gain insight into the necessity of using these techniques in order to obtain an improved estimate of the current density. MSR values were again calculated in order to quantify the impact of these techniques.

4.3 Results

4.3.1 Effects of Electrode Array Size

Figure 16 demonstrates the use of deconvolution upon a simple rotor. This figure shows the true current density, observed potential field, and deconvolved estimate of the current density at four time steps using a 20 x 20 array (a) and a 10 x 10 array (b). Deconvolution noticeably improves the estimate of the true signal with a large number of electrodes, a 20 x 20 array (a), and provides a less obviously, although still improved signal with the smaller array (b). Although improvements are not of the same caliber, with both array sizes deconvolution is able to provide resolution enhancement over the signal which is observed. This observation can be seen both with the simple rotor seen in Figure 16, as well as with a more complex activation pattern such as multi-wavelet reentry (Figure 17). Figure 17 demonstrates the utility of deconvolution upon activation patterns of this more complex signal at four time steps. Here, larger electrode arrays are used; a 30 x 30 array (a) and 15 x 15 array (b). These larger array sizes were necessary in order to obtain similar improvement as was found with the 20 x 20 and 10 x 10 arrays used to consider the simple rotor seen in Fig. 16. Improvements which can be made through deconvolution increase as array size is increased.

a.



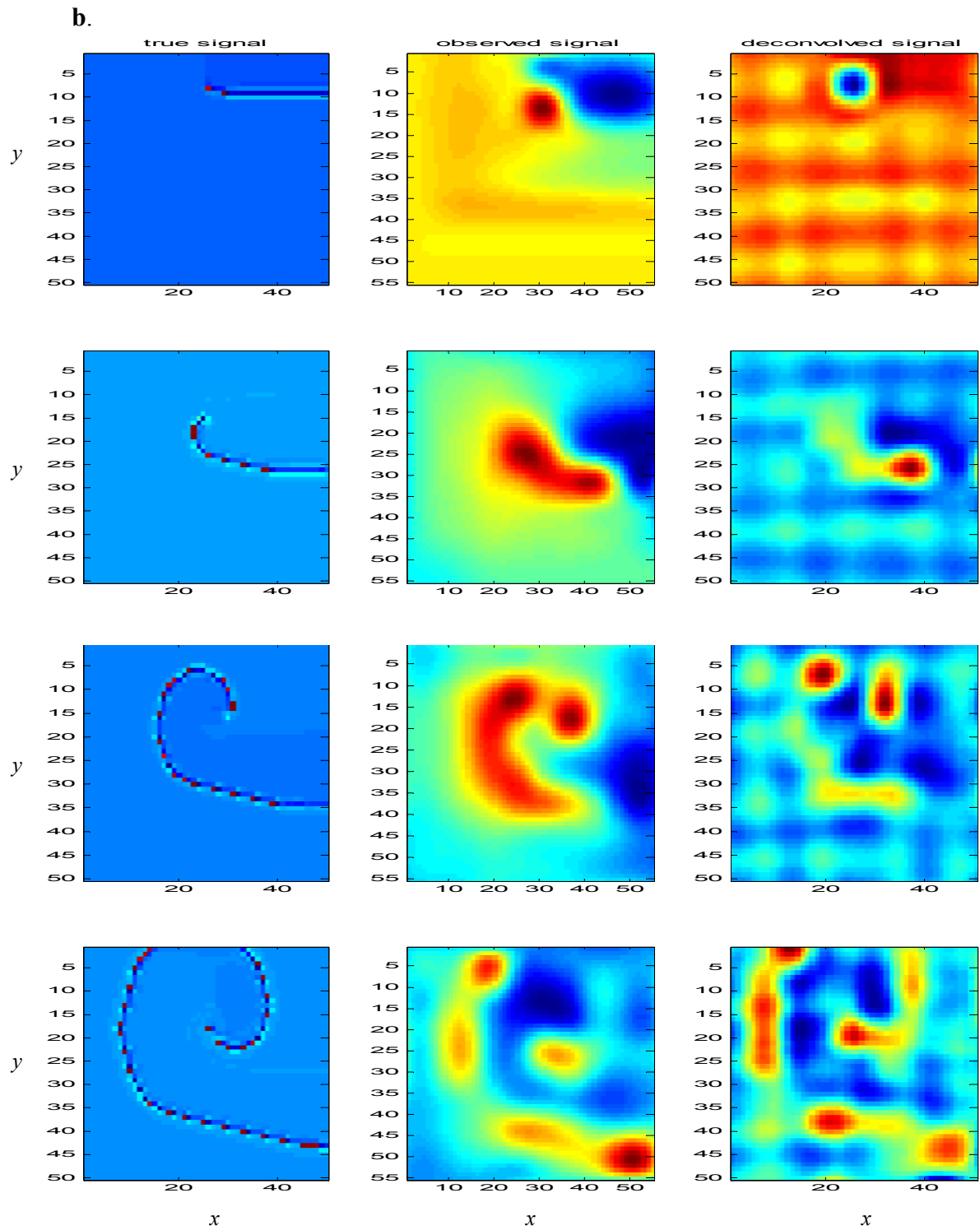
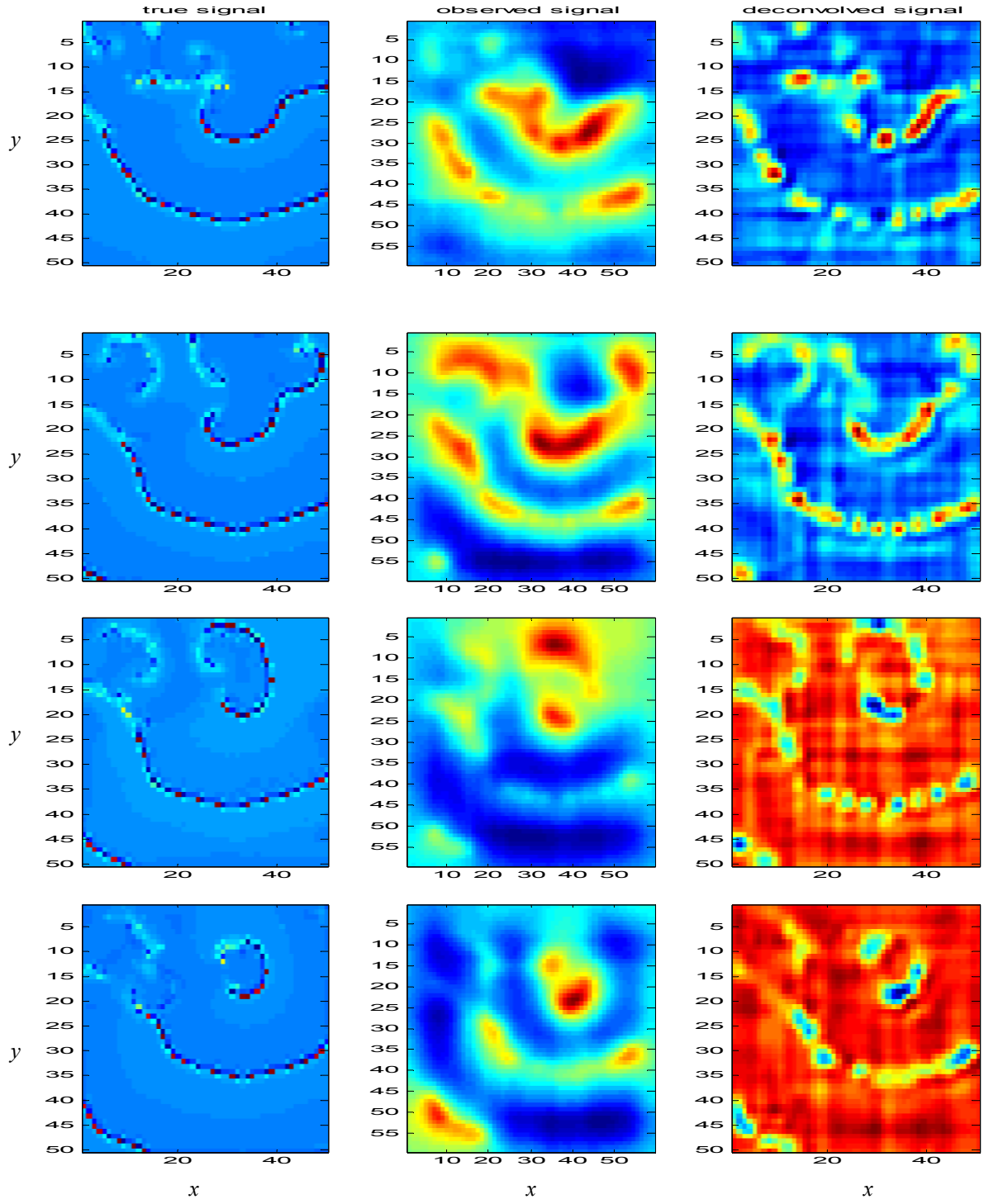


Figure 16. True current density, observed electrical potential, and deconvolved signal at multiple time steps using an electrode array of 20 x 20 (a) and 10 x 10 (b) at a height of 2. It is clear in both a and b that deconvolution provides an improved estimate of the current density and that with a larger array of electrodes this improvement is greater.

a.



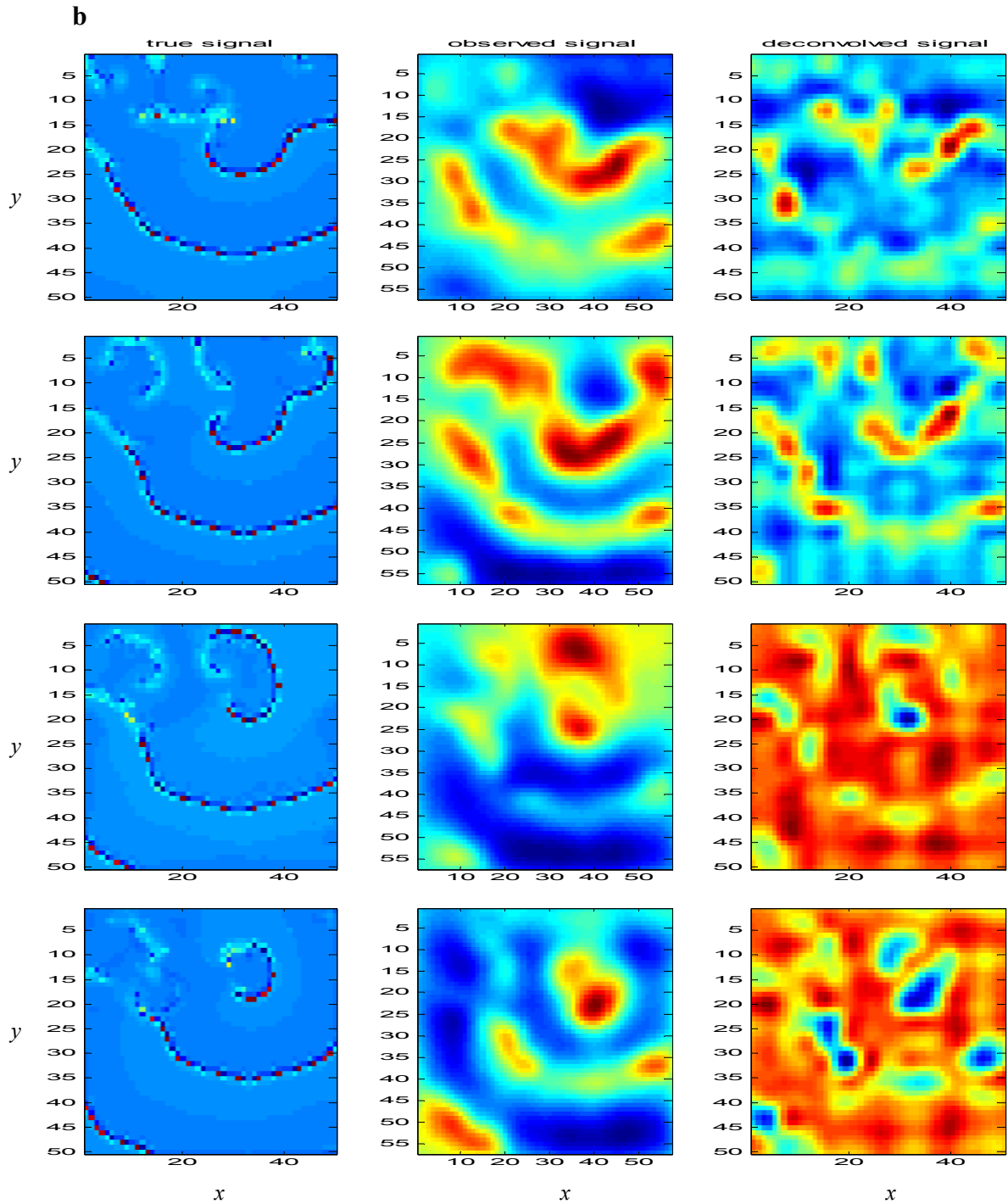


Figure 17. True current density, observed signal, and deconvolved signal using a 30 x 30 and 15 x 15 array of electrodes at a height of 2. It is clear that the deconvolved signal provides an improved estimate of the true current density and that this improvement increases as the number of electrodes is increased.

Calculation of MSR_{obs} and MSR_{dec} values provides a quantitative analysis of the improvements made through deconvolution (Figures 18, 19). Figure 18 shows MSR_{obs}

and MSR_{dec} corresponding to the four time steps of the simple rotor seen in Figure 16. These values give an indication of the impact of deconvolution upon the simple rotor as electrode spacing is varied. At most time steps, with an approximately 10 x 10 electrode array, deconvolution is able to provide an improved estimate of the current density. However, with a smaller electrode array, the use of deconvolution results in an estimate of the current density which is less similar to the true current density than the signal which is observed. At the first time step in Figure 18, regardless of the size of the electrode array being used, MSR_{obs} can be seen to be less than MSR_{dec} , showing deconvolution to not be useful.

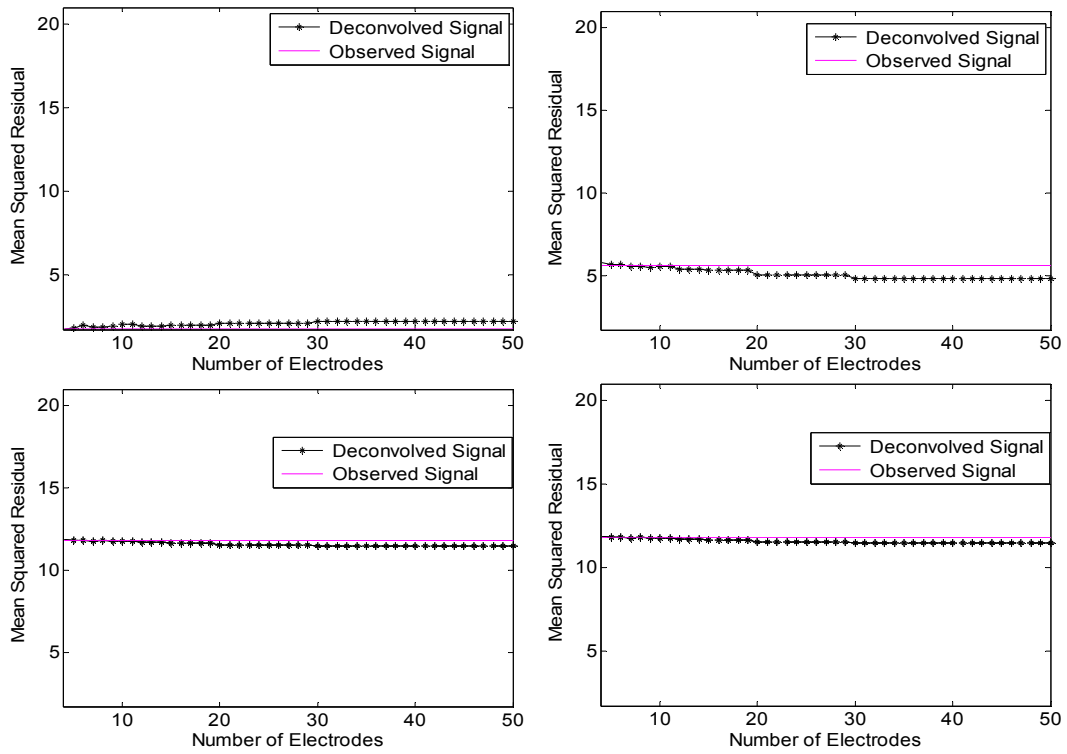


Figure 18. MSR comparing the observed and deconvolved signal with the true signal. This is calculated at the four time steps corresponding to the four time steps shown in Figure 16.

A similar result can be seen when considering multi-wavelet reentry (Figure 19).

Figure 19 provides MSR_{obs} and MSR_{dec} corresponding to the four time steps of multi-

wavelet reentry activation patterns seen in Figure 17. At most time steps deconvolution is able to provide an improved result. However, at the third time step MSR_{dec} is again greater than MSR_{obs} , showing the deconvolved signal to be less similar to the true current density than what is observed. MSR calculations at the other time steps show an improvement through deconvolution with a relatively small number of electrodes, less than a 10 x 10 array. If a smaller array is used than this threshold amount, it can be seen that MSR_{obs} has a smaller value and is therefore a better estimate of the true current density than that found through deconvolution. Figures 18 and 19 indicate that with both these signals, at the fixed electrode height considered, this necessary number of sensing electrodes is low, less than a 10 x 10 array, with the exception of the time steps for which deconvolution does not prove useful.

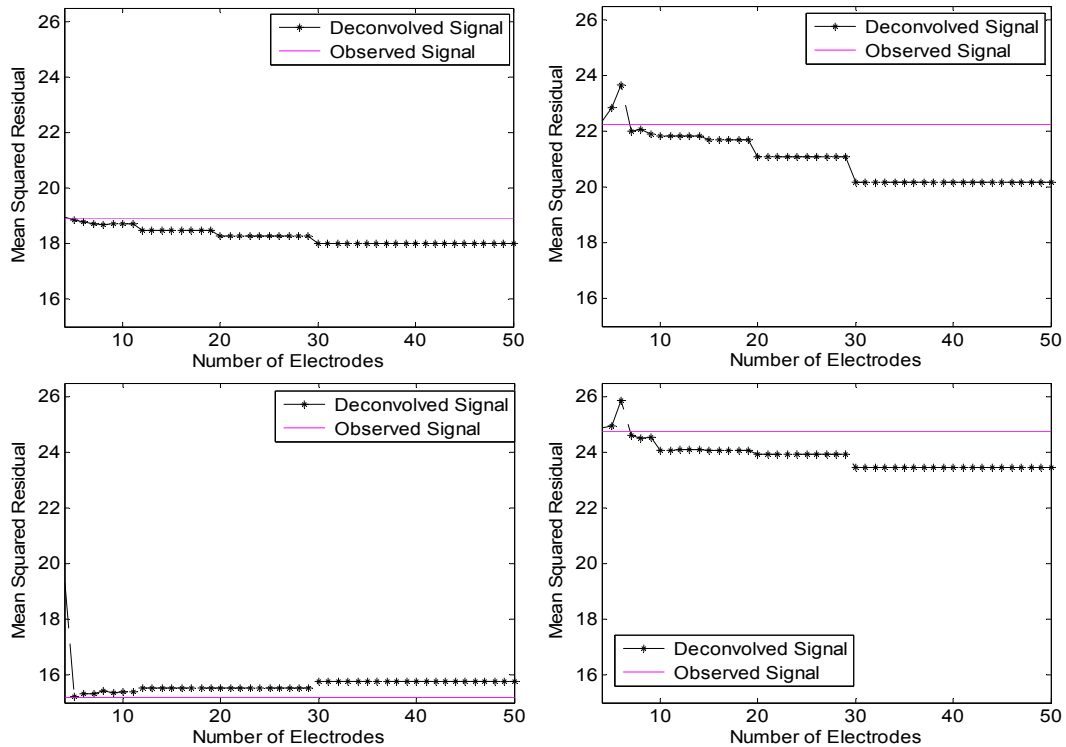


Figure 19. MSR comparing the observed and deconvolved signal with the true signal. This is calculated at the four time steps corresponding to the four time steps shown in Figure 17.

4.3.2 Effects of Electrode Height

Figure 20 demonstrates the observed potential field when electrode height is increased from 1 to 5 to 10. It is clear that as electrode height is increased, the blurring effect of convolution has an increased impact. The observed signal becomes increasingly imprecise and has a pattern which is clearly much less distinguished. Comparison the left image, the signal observed at a height of 1, to the right image, recorded at a height of 10 demonstrates that at a height of 10 the rotor which can be seen in the left image is no longer apparent.

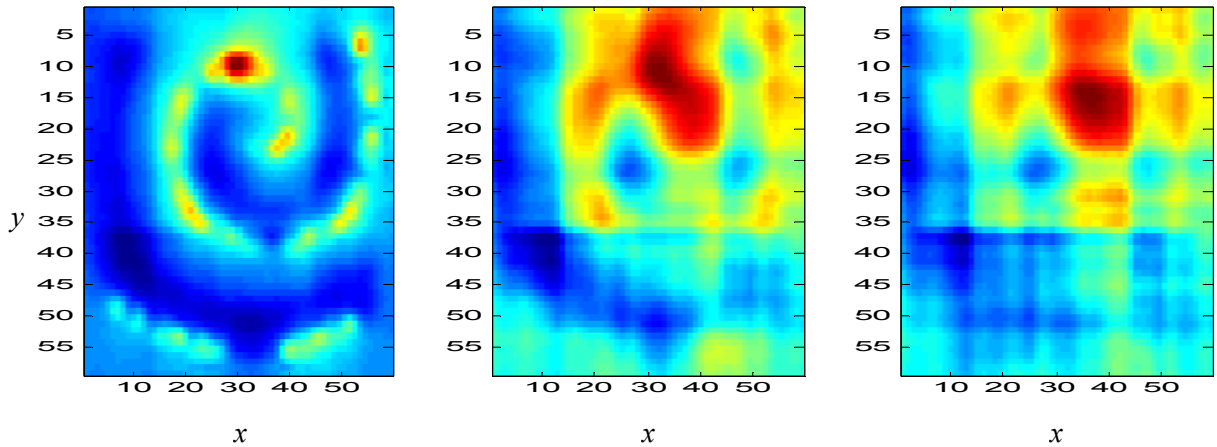


Figure 20. Observed signal at heights of 1, 5, and 10, it is clear that as the height of the electrode array is increased, the signal which is observed becomes increasingly blurred.

Figure 21 shows the effect of increasing electrode height upon both the observed and deconvolved signals. Here, as we increase height, recording the same signal with the same number of sensing electrodes, both the observed and deconvolved signals become increasingly blurred. The increased electrode height causes deterioration in signal resolution which can be provided through deconvolution. However, it can be noted when

considering these signals that even at a height of 5 the deconvolved signal is more similar to the true signal than the signal observed by the array of electrodes.

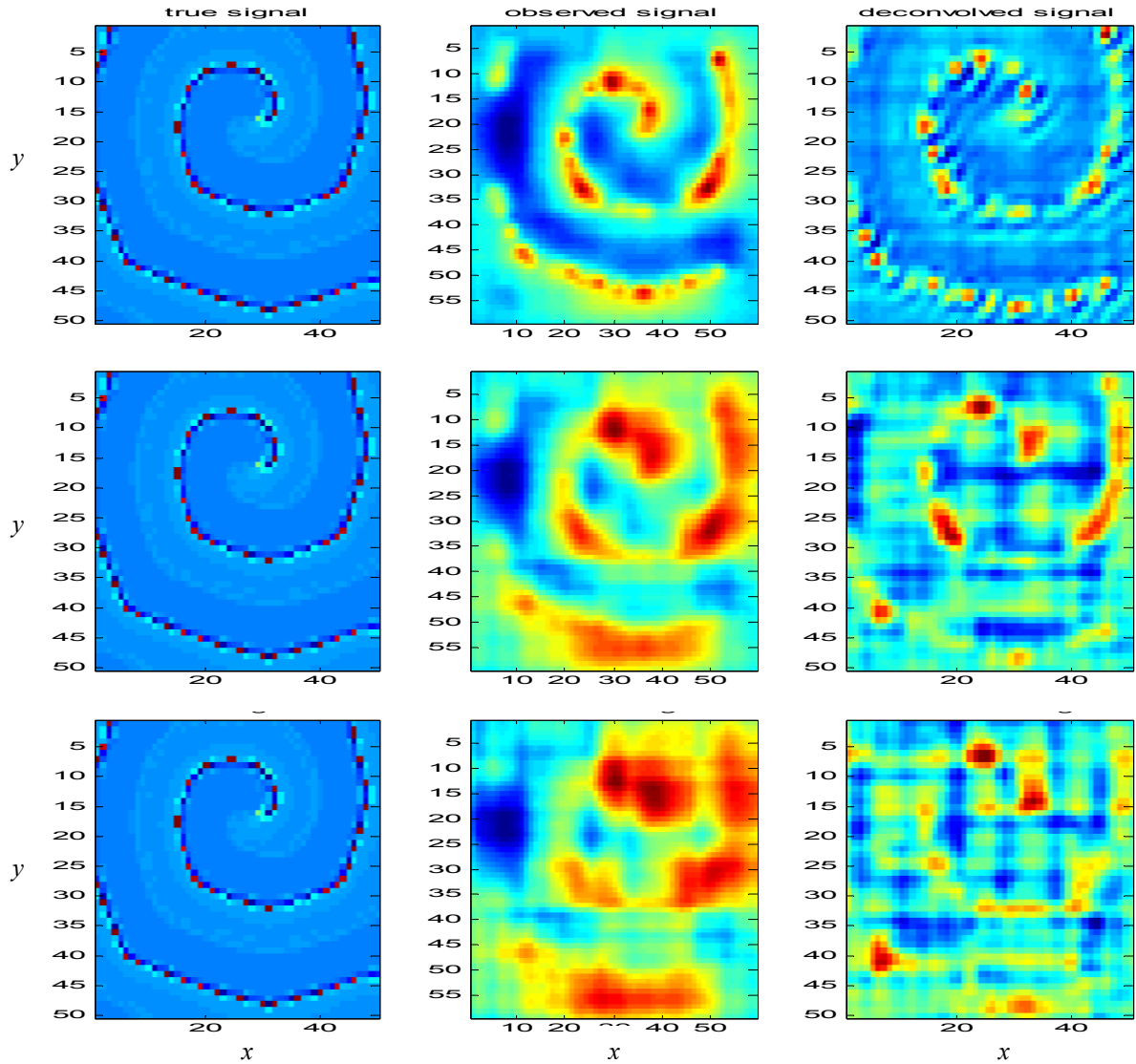


Figure 21. True current density, observed signal, and deconvolved signal at heights of 1 (top), 3 (middle), and 5 (bottom). It is clear that as the height of the electrode array is increased, the signal which is observed becomes increasingly blurred and in turn the deconvolved signal also looks increasingly blurred.

MSR calculations were used to quantify the influence of electrode height which is clearly evident through observation of the signals. Figure 22 depicts MSR_{obs} and MSR_{dec} values calculated at electrode heights of 1, 3, 5, and 10. At low electrode heights deconvolution provides a signal which is more similar to the true signal than what is observed. This improvement due to deconvolution deteriorates as electrode height is increased and finally, at a height of 10, deconvolution does not provide an improved estimate of the true current density and MSR_{dec} is greater than MSR_{obs} regardless of number of electrodes in the array used.

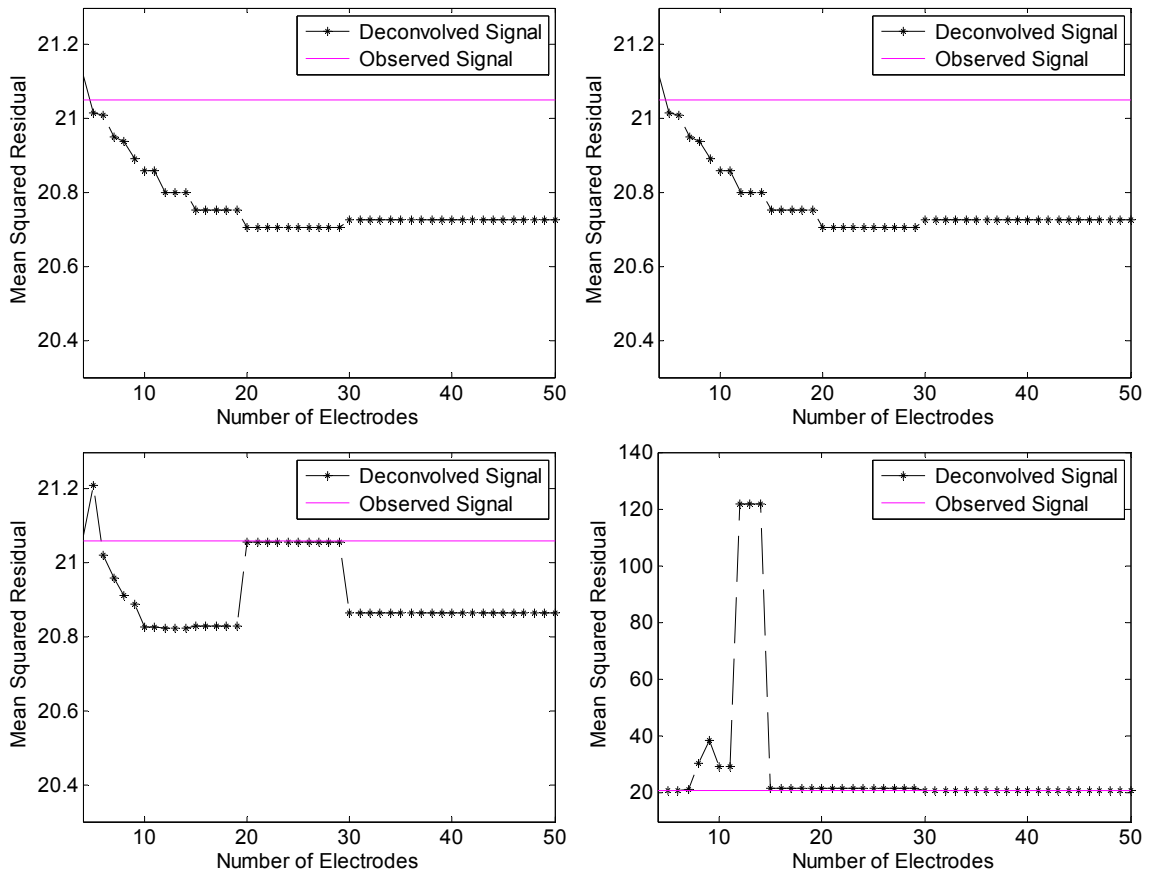


Figure 22. Mean squared residual of the same signal at heights of 1 (top left), 3 (top right), 5 (bottom left), and 10 (bottom right). It is clear that as the height of the electrode array is increased the observed signal becomes increasingly blurred and further that deconvolution becomes less useful in providing an improved estimate of the true signal.

4.3.3 Effects of Edge Extension

As was seen in Figure 15, we use of edge extension and windowing on the partial potential field to smoothly extend the observed map to zero without losing a large portion of the observed data. Figure 23 demonstrates the use of deconvolution upon the a truncated potential field prior to the use of edge extension and windowing (a), after smooth edge extension (b) and after edge extension in combination with windowing (c). When a partial version of a convolved signal is considered and edge extension is not used (a), the deconvolved signal has significant noise and does not look similar to the true signal. Part b of Figure 23 provides an estimate of the current density which is more similar to the true current density than prior to the use of edge extension; however this is still a poor estimate. The use of edge extension followed by windowing (c) provides a deconvolved signal which is much more like the true current density than seen prior to these procedures. It can be noted through examination of the three panels of this figure that the application of both edge extension and multiplication by the window provides a deconvolved signal with a much greater resolution than prior to the use of these procedures.

Figure 24 compares MSR_{obs} and MSR_{dec} values prior to the use of edge extension and windowing with MSR_{obs} and MSR_{dec} after these techniques have been used. When no edge extension and no windowing are used on the observed signal (top left), deconvolution is unable to provide an improved estimate of the true signal. Further, when edge extension but no window is applied to the observed signal prior to deconvolution (top right), the deconvolved signal again does not exhibit an improvement over the observed signal. However, when both edge extension and the window are

applied to the observed signal prior to deconvolution, the deconvolved signal exhibits a significant improvement over the observed signal. This gives a clear indication that the use of these techniques is necessary in order to provide enhancement of resolution through deconvolution.

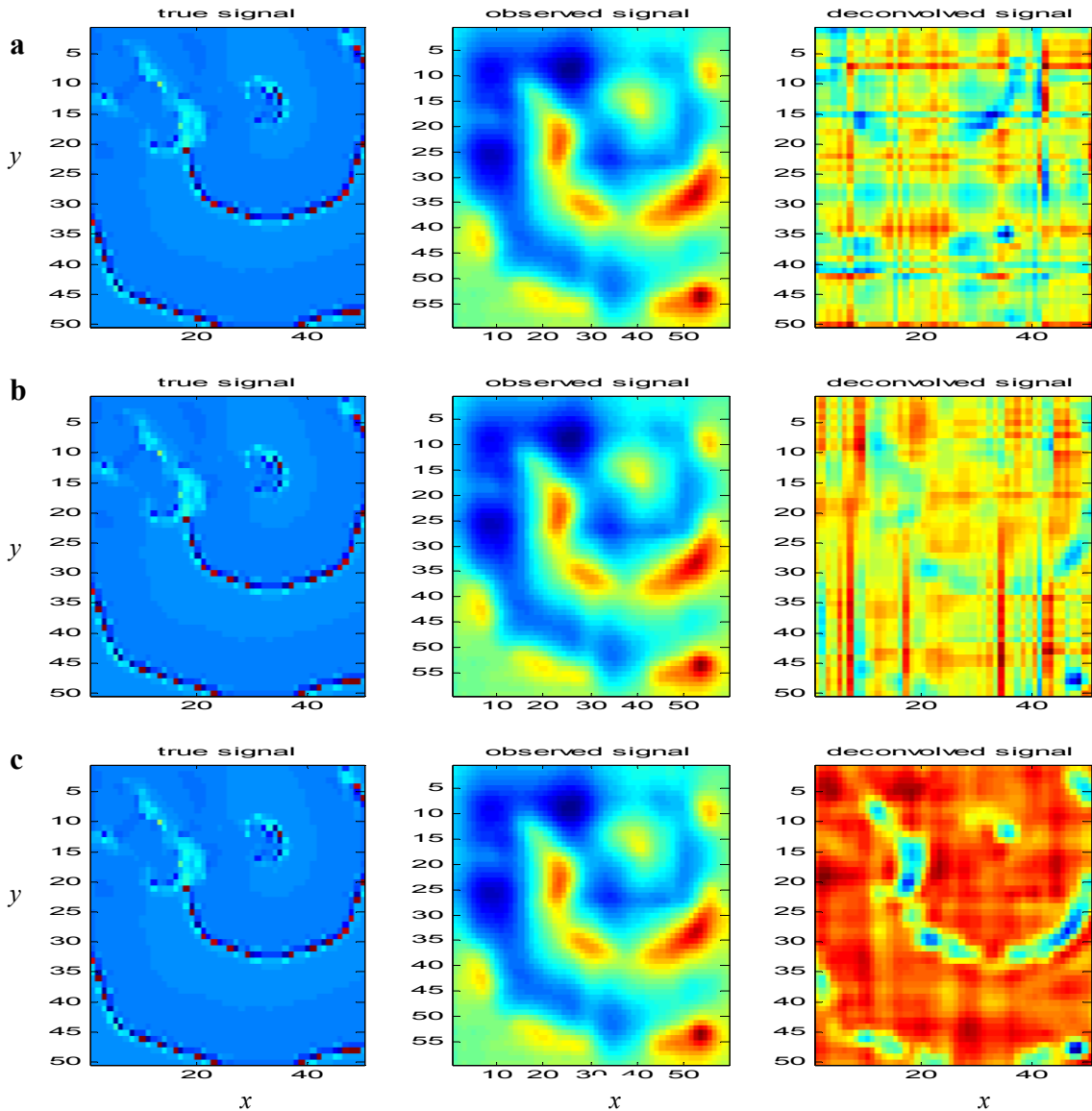


Figure 23. Deconvolution from a partial convolved signal with no edge extension (a) edge extension but no windowing (b) and edge extension and windowing (c). It is evident that the use of edge extension and windowing provides a much improved deconvolved signal.

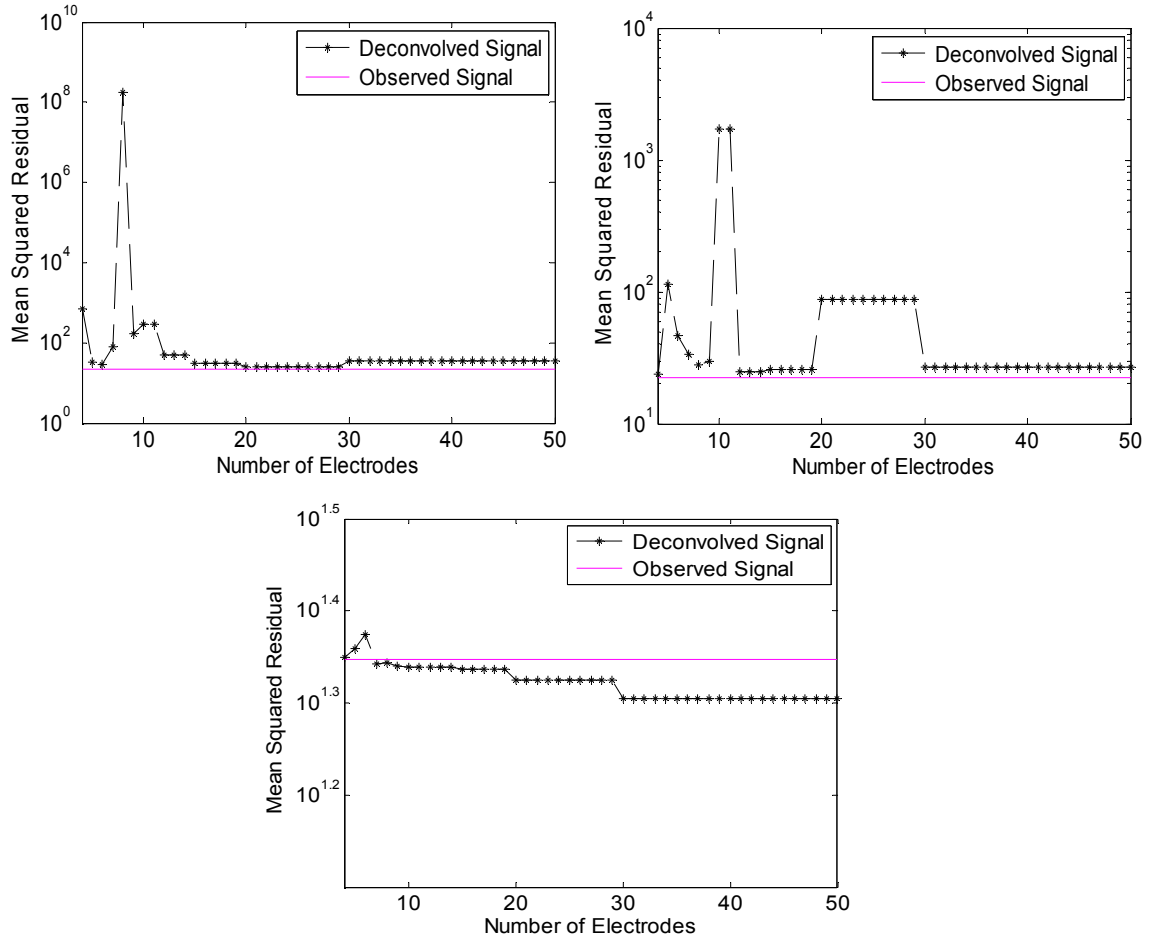


Figure 24. Mean squared residual calculations considering the same signal with no extension and no windowing, extension and no windowing, and extension and windowing. It is clear that the use of edge extension as well as a window provides a signal upon which deconvolution can be used in order to provide an improved estimate of the true signal.

4.4 Discussion

The results of deconvolution in two dimensions clearly indicate that with a necessary number of sensing electrodes, deconvolution is useful in providing an improved estimate of the true current density. Figure 16 demonstrates that deconvolution gives a signal which is more similar to the true current density than what is observed. Through consideration of the series of time steps shown, it can be clearly seen that the deconvolved signal resembles the rotor seen in the images of the true current density

while the observed signal displays an obviously blurred version. Comparison of the signals found using a 20 x 20 array (a) and a 10 x 10 array (b) demonstrates that deconvolution provides a greater improvement with the larger array. However, it is evident that the deconvolved estimate is still more similar to the true current density with the 10 x 10 array. This improvement can also be seen through the MSR calculations seen in Figure 18. It can be seen at most time steps that an improvement is made with a small number of electrodes. However, in the first image, which calculates the residual for the top panel in Fig. 16, deconvolution does not cause improvement. This result is likely due to the fact that at this time step only a few points exhibit current in the true current density field. This then means that when the deconvolved signal exhibits more current it has a larger effect upon MSR calculations. In this instance, therefore, this calculation is not the best indication of improvements made through deconvolution.

Figure 17 furthers the results seen in Figure 16, demonstrating the utility of deconvolution with a more complex activation pattern, multi-wavelet reentry. It is clear as this sequence of time steps is examined that deconvolution provides a signal much more similar to the true current density than that which is observed. It is evident when sampled with a 30 x 30 array (a) that activation patterns seen in the true signal but which are not evident in the observed signal can be recovered through deconvolution. Such a result can be seen when sampling with a 15 x 15 array (b) to a lesser degree. By viewing a series of time steps a greater indication of the activation patterns can be seen when looking at the deconvolved estimate of the current density than when considering the observed potential field. MSR calculations, shown in Figure 19, in most cases indicate an improvement. Further, this improvement is seen with a small number of electrodes,

and clearly increases as the number of electrodes increases. This correlates well with the result seen through the observations which were made when considering images of deconvolved signals. However, the third panel of Figure 19 does not indicate an improvement through deconvolution. This does not correlate to the result seen in the third panel of Fig. 17, which shows a clearly more similar deconvolved signal when compared to the true current density. This result indicates that the MSR calculations may not be the best indicator of the improvements which can be made through deconvolution. At the low height used, consideration of both the simple rotor as well as multi-wavelet reentry indicates that with a small electrode array, less than 10 x 10, deconvolution can begin to provide an improved estimate of the true current density. It is evident, however, that this improvement is not as great with a more complex signal and for such an activation pattern using approximately a 15 x 15 array of electrodes would provide a more clear improvement through deconvolution.

Electrode height has a great effect on both the observed potential field as well as the deconvolved estimate of the current density. Figure 20 shows the observed signal as height is increased. It is quite obvious when looking at the three images that the signal becomes increasingly blurred as electrode height is increased, and no longer resembles the rotor which is being recorded. Figure 21 demonstrates that as the observed signal becomes increasingly blurred the utility of deconvolution begins to decrease. It is evident that with a greater electrode height the deconvolved signal is less similar to the true current density than with a lower height. However, it is clear that, even at a height of 5, although less significantly, deconvolution is able to provide improved signal resolution. As shown in Figure 22 calculation of MSR values clearly indicates that if a very large

electrode height is used, deconvolution no longer causes improvements in signal resolution. It is evident here that as electrode height is increased, improvements due to deconvolution begin to deteriorate as we observed in Figure 21. With electrode heights of 1, 3, and 5, deconvolution continues to provide a signal more similar to the true current density than the observed signal, as was seen in Figure 21. However, at a height of 10, deconvolution is no longer able to improve our estimate of the current density. At such a great sensing height, even with a large number of electrodes, deconvolution no longer proves useful. It is therefore evident that the sensing electrode must be at a height of approximately 5 or lower in order to allow deconvolution to prove useful.

Edge extension and windowing are important tools which often prove necessary when utilizing deconvolution through Fourier transforms [39]. Figure 15 shows that our use of a combination of windowing and edge extension cause the observed potential field to smoothly extend to zero while retaining much of its original shape. The effects of these techniques are shown in Figure 23, which clearly demonstrates that prior to the use of this combination of methods (a, b) there is a large amount of noise in the deconvolved signal. However, when the observed signal is both extended and windowed (c) deconvolution is able to provide a less noisy signal which is an improved estimate of the true current density field. This improvement can be confirmed when considering MSR values seen in Figure 24. These results, which show an improvement only when both edge extension and windowing are applied, confirm that these techniques are necessary in order to allow deconvolution to be a useful tool in providing an improved estimate of the true current density.

It can be seen that the reductions seen in MSR values due to deconvolution are of a small percentage and do not show a greatly significant change. When considered alone, MSR reductions may therefore seem as if they are not practically significant. However, when considered in conjunction with images of deconvolved signals, the significance of the improvements due to deconvolution increases. When a series of time steps of deconvolved signals are considered, it can be clearly seen that the deconvolved signal looks more similar to the true current density than what was observed. If an experienced observer was to consider these images of the deconvolved signal, it is likely they would have a clear view of the activation pattern occurring in the tissue. Although this is a result which can not be quantified and relies upon the observer, it is clear that when a series of images of the deconvolved signal is considered, an improvement can be seen through deconvolution. This result could easily be applied in a practical way as observation of the deconvolved signal could be used to provide an improved view of the activation patterns of the heart during AF.

The results of this study of deconvolution provide a similar indication to those found by Chouvarda et al who also studied the utility of deconvolution in improving multi-electrode array electrogram recordings. Similarly to our work, their study clearly found that with a sufficiently dense electrode array, using sensing electrodes a small distance from the tissue, deconvolution was able to provide improved signal resolution. Their study, however, did not consider the effect of electrode height upon the utility of deconvolution. Further, they did not consider that the electrodes would record only a partial version of the potential field, and so did not make use of windowing or edge extension [11]. Our work expands on the ideas exhibited Chouvarda et al by including

considerations of the impact of electrode height as well as the impact of sampling a partial version of the potential field. This therefore allows the results of the current study to have a more widespread application, and further emphasizes the utility of deconvolution in improving the observed potential field.

It is evident that this study of the utility of deconvolution is limited by a number of assumptions which were made. By using simulated data from a cellular automaton model of atrial activation patterns, we have used assumptions which were made in this model by Spector et al [43]. Further, we assume that we are using arrays of point electrodes at known heights. If this technique was applied to recordings taken from atrial tissue, the electrodes would have diameter which could influence the impacts of deconvolution. Further, the exact electrode height would likely not be known when mapping the atria as is assumed in this study. Finally, we make an assumption that the tissue can be considered to be two dimensional which may not apply to many situations of actual mapping of activation patterns in the atria.

Although limited in this sense, this study has indicated that using an electrode array of approximately 10 x 10 electrodes or greater sensing at a height of approximately 5 or less, deconvolution is able to provide an improved estimate of the true current density. The use of these techniques would allow for a greater ability for the electrophysiologist to map the electrical activity of the atria during AF, which could lead to a better use of catheter ablation.

In order to further this study, it will be necessary consider the limitations that are seen in the present study. Because we are currently considering point electrodes, it will be important to consider the effects that electrode diameter has on both the observed

signal as well as the utility of deconvolution. Further, if one was performing a mapping procedure it is unlikely they would know the exact height of the sensing electrode causing study upon the effect of the electrode height being unknown is necessary. We have briefly considered the impact of using a varied electrode height upon the deconvolved signal and have found that this issue can likely be overcome. However, this needs to be considered in a greater sense and quantified in order to have a clear understanding of the practical utility of this procedure. Furthermore, analyzing the utility of deconvolution in three dimensions would provide a greater understanding of the ability to use this technique in a clinical setting. To further this understanding, simulating the ablation pattern which our deconvolved signal implicates upon the simulated current density field would give an indication of the efficacy of this method in providing improved ablation techniques. Finally, an experimental application of deconvolution upon an observed potential field in an animal model would be a necessary final step. This application would allow us to not only use deconvolution to improve signal resolution, but also allow for our result to be used in order to determine an ablation pattern which could be used. Such applications would clearly indicate the use of this technique in improving ablation procedures and terminating AF.

Chapter Five: Conclusions

In this study we have evaluated the utility of deconvolution in providing an improved estimate of the current density field which occurs in atrial tissue during AF. Through the use of simulated recordings of atrial activation, we have made use of deconvolution in order to estimate the true current density in both one and two dimensions. The simulation of increasingly complex activation patterns has allowed us to gain insight into the power of deconvolution in providing a signal which is more similar to the current density field occurring within the tissue than what is observed by an array of sensing electrodes. It is apparent that under specified circumstances deconvolution proves a useful tool in providing an improved estimate of atrial activation patterns.

The observations made through our study indicate that our use of edge extension techniques provides a significantly improved signal when we use deconvolution upon a partial version of the potential field. Because an electrode array would not cover the entire extent of the atrial tissue and would record a truncated version of the potential field, it is evident that the use of these techniques is necessary in order to employ deconvolution. Further, when utilizing these techniques, our results point towards a need to use an approximately 10 x 10 or greater array of electrodes at a relatively low sensing height. It is clear that by increasing this array size a greater improvement in signal resolution can be obtained through the use of deconvolution. When mapping a more complex activation pattern, it is likely that using a 10 x 10 electrode array will provide a relatively small improvement while using a 15 x 15 array would provide a more significantly improved signal resolution and allow a clear view of the excitation pattern

of the atrial tissue, implicating a need to consider the use of this larger array size. Such application of deconvolution to the electric potential which is recorded through simultaneous intra-atrial mapping could provide the insight necessary to allow for individualized ablation plans for patients being treated for AF. This would allow for increased success rates in eliminating the arrhythmia through ablation procedures which would in turn reduce medical issues for an increasing number of patients suffering from AF.

In future work, the practical limitations which are not currently considered need to be studied. The impact of electrode diameter upon the observed signal and its impact on the utility of deconvolution must be considered. Further, it is important to consider recordings made at an imprecise electrode height and improvements which can be made through deconvolution in such a situation. Finally this problem needs to be considered in three dimensions and eventually upon actual electric potential recordings made from an animal model in order to provide a clear indication of the practical utility this technique of resolution enhancement.

References

1. Nair, G.M., et al., *A systematic review of randomized trials comparing radiofrequency ablation with antiarrhythmic medications in patients with atrial fibrillation*. J Cardiovasc Electrophysiol, 2009. **20**(2): p. 138-44.
2. Singla, S., et al., *Review of Contemporary Antiarrhythmic Drug Therapy for Maintenance of Sinus Rhythm in Atrial Fibrillation*. J Cardiovasc Pharmacol Ther.
3. Go, A.S., et al., *Prevalence of diagnosed atrial fibrillation in adults: national implications for rhythm management and stroke prevention: the AnTicoagulation and Risk Factors in Atrial Fibrillation (ATRIA) Study*. Jama, 2001. **285**(18): p. 2370-5.
4. Savelieva, I., et al., *Upstream therapies for management of atrial fibrillation: review of clinical evidence and implications for European Society of Cardiology guidelines. Part I: primary prevention*. Europace. **13**(3): p. 308-28.
5. Allesie, M.A., et al., *Electrophysiologic mechanisms of perpetuation of atrial fibrillation*. Am J Cardiol, 1996. **77**(3): p. 10A-23A.
6. Labrova, R., J. Spinar, and N. Honzikova, *Radiofrequency ablation in treatment of atrial fibrillation*. Physiol Res. **59 Suppl 1**: p. S43-9.
7. Ames, A. and W.G. Stevenson, *Catheter Ablation of Atrial Fibrillation*. Circulation, 2006. **113**(13): p. e666-e668.
8. Rostock, T., et al., *Long-term single- and multiple-procedure outcome and predictors of success after catheter ablation for persistent atrial fibrillation*. Heart Rhythm. **8**(9): p. 1391-7.
9. Habel, N., et al., *The temporal variability of dominant frequency and complex fractionated atrial electrograms constrains the validity of sequential mapping in human atrial fibrillation*. Heart Rhythm. **7**(5): p. 586-93.
10. Bates, J.H. and P.S. Spector, *On the ill-conditioned nature of the intracardiac inverse problem*. Conf Proc IEEE Eng Med Biol Soc, 2009. **2009**: p. 3929-31.
11. Chouvarda, I., et al., *Deconvolution and wavelet-based methods for membrane current estimation from simulated fractionated electrograms*. IEEE Trans Biomed Eng, 2001. **48**(3): p. 294-301.
12. Levy, M.N., A.J. Pappano, and M.T. Nelson, *Cardiovascular Physiology*. Ninth ed. 2007, New York: Mosby.
13. Tsiperfal, A., *Cardiac arrhythmia management :a practical guide for nurses and allied professionals*. 2011, Chichester, West Sussex, UK :: Wiley-Blackwell. xx, 494 p. .:
14. Zipes, D.P., J.e. Jalife, and *Cardiac electrophysiology :from cell to bedside*. 5th ed. ed. 2009, Philadelphia, PA Saunders/Elsevier. xxv, 1155 p. .:
15. Vigmond, E.J., R. Ruckdeschel, and N. Trayanova, *Reentry in a morphologically realistic atrial model*. J Cardiovasc Electrophysiol, 2001. **12**(9): p. 1046-54.
16. University of Toronto, C.o.M. *Atrial Fibrillation Teaching File*. 2008 <http://afib.utorontoeit.com/index.html>.

17. Viles-Gonzalez, J.F., et al., *Rhythm control for management of patients with atrial fibrillation: balancing the use of antiarrhythmic drugs and catheter ablation*. Clin Cardiol. **34**(1): p. 23-9.
18. Boriani, G., et al., *Pharmacological cardioversion of atrial fibrillation: current management and treatment options*. Drugs, 2004. **64**(24): p. 2741-62.
19. Bollmann, A. and F. Lombardi, *Electrocardiology of atrial fibrillation. Current knowledge and future challenges*. IEEE Eng Med Biol Mag, 2006. **25**(6): p. 15-23.
20. Nademanee, K., et al., *Catheter ablation of atrial fibrillation guided by complex fractionated atrial electrogram mapping of atrial fibrillation substrate*. J Cardiol. **55**(1): p. 1-12.
21. Yu, L., et al., *Interactions between atrial electrical remodeling and autonomic remodeling: How to break the vicious cycle*. Heart Rhythm.
22. Dang, L., et al., *Evaluation of ablation patterns using a biophysical model of atrial fibrillation*. Ann Biomed Eng, 2005. **33**(4): p. 465-74.
23. Parkash, R., et al., *Approach to the Catheter Ablation Technique of Paroxysmal and Persistent Atrial Fibrillation: A Meta-Analysis of the Randomized Controlled Trials*. J Cardiovasc Electrophysiol.
24. Eckstein, J., et al., *Mapping of atrial fibrillation--basic research and clinical applications*. Swiss Med Wkly, 2009. **139**(35-36): p. 496-504.
25. Lemery, R., *Bi-atrial mapping of atrial arrhythmias*. Card Electrophysiol Rev, 2002. **6**(4): p. 378-82.
26. Derakhchan, K., et al., *Method for simultaneous epicardial and endocardial mapping of in vivo canine heart: application to atrial conduction properties and arrhythmia mechanisms*. J Cardiovasc Electrophysiol, 2001. **12**(5): p. 548-55.
27. Konings, K.T., et al., *Configuration of unipolar atrial electrograms during electrically induced atrial fibrillation in humans*. Circulation, 1997. **95**(5): p. 1231-41.
28. Jacquemet, V. and C.S. Henriquez, *Genesis of complex fractionated atrial electrograms in zones of slow conduction: a computer model of microfibrosis*. Heart Rhythm, 2009. **6**(6): p. 803-10.
29. Oral, H., et al., *A randomized assessment of the incremental role of ablation of complex fractionated atrial electrograms after antral pulmonary vein isolation for long-lasting persistent atrial fibrillation*. J Am Coll Cardiol, 2009. **53**(9): p. 782-9.
30. Atienza, F., et al., *Real-time dominant frequency mapping and ablation of dominant frequency sites in atrial fibrillation with left-to-right frequency gradients predicts long-term maintenance of sinus rhythm*. Heart Rhythm, 2009. **6**(1): p. 33-40.
31. Verma, A., et al., *Relationship Between Complex Fractionated Electrograms (CFE) and Dominant Frequency (DF) Sites and Prospective Assessment of Adding DF-Guided Ablation to Pulmonary Vein Isolation in Persistent Atrial Fibrillation (AF)*. J Cardiovasc Electrophysiol.
32. Hall, P. and P. Qiu, *Nonparametric estimation of a point-spread function in multivariate problems*. Ann. Statist., 2007. **35**(4).

33. Bracewell, R.N., *The Fourier Transform and Its Applications*. Second ed. 1978, New York: McGraw-Hill Book Company.
34. Peters, T.M., J. Williams, and J.H.T. Bates, *The Fourier transform in biomedical engineering*. 1998, Boston: Brickhauser.
35. Weisstein, E.W. *Convolution*. <http://mathworld.wolfram.com/Convolution.html>.
36. Press, W.H., et al., *Numerical Recipes The Art of Scientific Computing*. 1986, New York: Cambridge University Press.
37. Bányász, Á., G. Dancs, and E. Keszei, *Optimisation of digital noise filtering in the deconvolution of ultrafast kinetic data*. Radiation Physics and Chemistry. **74**(3-4): p. 139-145.
38. Bates, J.H.T., W.R. Fright, and R.H.T. Bates, *Wiener filtering and cleaning in a general image processing context*. Monthly Notices of the Royal Atromical Society, 1984. **211**(114).
39. Harris, F.J., *On the use of windows for harmonic analysis with the discrete Fourier transform*. Proceedings of the IEEE, 1978. **66**(1): p. 51-83.
40. Smith, S.W., *The Scientist and Engineer's Guide to Digital Signal Processing*. 1997, California Technical Publishing: San Diego, CA.
41. Jacquemet, V., et al., *Study of unipolar electrogram morphology in a computer model of atrial fibrillation*. J Cardiovasc Electrophysiol, 2003. **14**(10 Suppl): p. S172-9.
42. Blanc, O., et al., *A computer model of human atria with reasonable computation load and realistic anatomical properties*. IEEE Trans Biomed Eng, 2001. **48**(11): p. 1229-37.
43. Spector, P.S., et al., *Emergence of complex behavior: an interactive model of cardiac excitation provides a powerful tool for understanding electric propagation*. Circ Arrhythm Electrophysiol. **4**(4): p. 586-91.
44. Wiener, N. and A. Rosenblueth, *The mathematical formulation of the problem of conduction of impulses in a network of connected excitable elements, specifically in cardiac muscle*. Arch Inst Cardiol Mex, 1946. **16**(3): p. 205-65.
45. Moe, G.K., W.C. Rheinboldt, and J.A. Abildskov, *A Computer Model of Atrial Fibrillation*. Am Heart J, 1964. **67**: p. 200-20.
46. Bates, J., *Lung Mechanics: an Inverse Modeling Approach*. 2009, Cambridge, UK: Cambridge University Press.

Appendices

A. One Dimensional Deconvolution Code

This code is used to perform deconvolution in one dimension. The electrode height and number of electrodes can be changed in order to simulate varied mapping conditions in order to obtain an indication of the utility of deconvolution in each instance.

```
N = 900; % size of space
H = 1; % height
E = 100; % number of electrodes

Cs = CS8(500:650);

F = zeros (N+3100,1); % true signal
for J = 925:1075;
    F(925:1075) = Cs;
end

G = zeros (N+3100,1); % point spread function
for J = 1:N+1100
    G(J) = 1/(sqrt((J-900)^2 + (H^2)));
end

W = trapz(G);
G = G./W;

I = conv(F,G); % convolved
function

IS = zeros (N+3100,1);
for J = 1:N+800;
    IS(J) = I(J+900);
end

figure;
plot (G);
hold all
plot (F,'m');
plot (IS,'k');
legend('Point Spread Function','True Signal','Convolved
Signal','Location','NorthEast')
title ('Convolved');

%calculating electrode locations
T = zeros (1,E+1); % (N/E)*K
for K = 1:E;
```

```

    T(K) = ((N+3100)/E)*K; % electrode
positions
end

R = zeros (E+1,1); % calculating
I((N/E)*K)
for K = 1:E;
    R(K) =I(ceil(T(K)));
end

%calculating cubic spline
x = ceil(T);
y = R;
cs = spline(x,y);
a = ppval(cs,1:4000);
a1= a';

figure;

plot (I, 'k');
hold on,
plot(x,y, 'o'),
plot (a1, 'm');

legend ('Convolved', 'Electrodes', 'Cubic Spline')
title ('Electrode Locations');

%calculating FFTs
for J = 1000
    G(J) = 1.3*G(J);
end

GT = fft(G); % fft point spread
IT = fft(I(1:4000)); % fft convolved
AT = fft(a1); % fft spline

%deconvolving using FFT

FT =AT./GT;
F6 = ifft(FT); % deconvolved
signal

figure;
plot (F, 'k');
hold all
plot (F6, 'b');
plot (IS, 'm');
legend ('True Signal', 'Deconvolved Signal', 'Convolved
Signal', 'Location', 'NorthEast')

%Calculating Mean Squared Residuals
scaleF6 = lscov(F6,F);
scaleI = lscov(IS,F);

```

```

F62 = F6 * scaleF6;
IS2 = IS * scaleI;

figure;
plot (F, 'k');
hold all;
plot (F62, 'b');
plot (IS2, 'm');
legend ('True Signal', 'Scaled Deconvolved Signal', 'Scaled Convolved
Signal');

MSRF = zeros (N+3100,1); % mean squared
residual deconvolved
for J = 1:N+3100;
    MSRF(J) = MSRF(J) + ((F(J) - (F62(J)))^2);
end

MSRI = zeros (N+3100,1); % mean squared
residual convolved
for J = 1:N+3100;
    MSRI(J) = MSRI(J) + ((F(J) - (IS2(J)))^2);
end

figure;
hold all;
plot (MSRI, 'b');
plot (MSRF, 'k');
title ('Residuals');
legend ('Residual Convolved Signal', 'Residual Deconvolved
Signal', 'Location', 'NorthEast');

ValueI = sum (MSRI(1:4000));
ValueF = sum (MSRF(1:4000));

%calculating electrode spacing
si = length(I);
space = ceil(4000/E);

%printing values
fprintf('Electrode Spacing = %g\n', space);
fprintf('Height = %g\n', H);
fprintf ('Number of Electrodes = %g\n', E);
fprintf('MSR of Convolved: %g\n', ValueI);
fprintf('MSR of Deconvolved: %g\n', ValueF);

```

B. Two Dimensional Deconvolution Code

This code is used to perform deconvolution in two dimensions using a current density field which is loaded from simulations with the cellular automata model. The user is able to vary electrode height and number of electrodes at a chosen time step in order to simulate varied mapping conditions. This provides an indication of the utility of deconvolution in each instance.

```
%2 D deconvolution

close all;
clear all;

%variables that are changed
%electrode height
H = 2;

% number electrodes (array size is ExE)
E = 30;

%time step
ts = 1420;
ts2 = ts+1;

%truncation of convolved signal (amount mult by pt spread fcn)
%(this is the amount of convolved signal not being seen by electrodes)
trunc = .4;

% load true signal
load data5.mat;

n = 50;
% true signal defined as F
F = rotor((ts-1)*n+1:(ts*n), 2:51);
Fnext = rotor((ts2-1)*n+1:(ts2*n), 2:51);

Fdiff = Fnext-F;

t1 = trapz(Fdiff);
s1 = sum(t1);
f = Fdiff;
[sF,ssF] = size(Fdiff);

figure;
surf(f);
colormap(hsv);
```

```

title('true signal','LineStyle','none');
shading interp

% creating point spread function
[J,K]= meshgrid(-sF/2:1:sF/2,-ssF/2:1:ssF/2);
G = (sqrt((J.^2) +(K.^2) + (H.^2))).^-1;

%convolving F and G
I = conv2(Fdiff,G);
t2 = trapz(I);
s2 = sum(t2);
i = I/s2;

%cutting off to consider part of full convolved signal
cutoff = ceil(trunc*length(G));
sI = length(I);
II = I(cutoff:sI-cutoff,cutoff:sI-cutoff);

t2 = trapz(II);
s2 = sum(t2);
ii = II/s2;
ii = II;

%convolved signal same size as true signal
If = conv2(Fdiff,G,'same');
t4 = trapz(If);
s4 = sum(t4);
iF = If/s4;

figure;
surf(ii);
colormap(hsv);
title('truncated convolved signal');

[si2,ssi2] = size(ii);

% electrode locations
T = ceil(si2/E);
T2 = ceil(ssi2/E);

[A,B]= meshgrid(1:T2:ssi2,1:T:si2);

R =ii(1:T:si2,1:T2:ssi2);

% plot of electrode locations

figure;
mesh (A,B,R);
colormap(hsv);
beta = -.5;
brighten(beta);
title ('electrode locations');

```

```

[A1,A2] = size(A);
a = A(A1,A2);

%spline interpolation between electrode locations
C = (1:a);
D = (1:a);
I2 = interp2 (A,B,R,C,D', 'spline');

%cos with square top window idea
p = .5;
[si,ssi] = size(I2);
[sg, ssg] = size(G);
sCos = 2*ceil(p*sg);
sCos2 =2*ceil(p*ssg);

[x,y]= meshgrid(-sCos/2:1:sCos/2,-sCos2/2:1:sCos2/2);
r = sqrt(x.^2+y.^2);

Cos = .5*(1+ cos(r*2*pi/sCos2));
Cos(r>(sCos2/2)) = 0;

[sC,ssC] = size(Cos);
half1 = ceil(sC/2);
half2 = ceil(ssC/2);

corner1 = Cos (1:half1,1:half2);
corner2 = Cos (1:half1, half2:ssC);
corner3 = Cos (half1:sC,1:half2);
corner4 = Cos (half1:sC, half2:ssC);
middle = ones (si-ceil(p*sg), ssi-ceil(p*ssg));
sm = size(middle)-1;

side1 = Cos (half1-1:half1,1:half2);
side2 = Cos (half1-1:half1, half2:ssC);
side3 = Cos (1:half1, half2-1:half2);
side4 = Cos (half1:sC, half1-1:half1);

for n = half2-1:half2+sm+1;
x4 = half1+sm:sC+sm;
y4 = n:n+1;
mult(x4,y4) = side4;
end

for n = half1-1:half1+sm+1;
x2 = n:n+1;
y2 = half2+sm:ssC+sm;
mult(x2,y2) = side2;
end

for n = half1-1:half1+sm-1;
x1 = n:n+1;

```

```

y1 = 1:half2;
mult(x1,y1) = side1;
end

for n = half2-1:half2+sm-1;
x3 = 1:half1;
y3 = n:n+1;
mult(x3,y3) = side3;
end

mult(1:half1,1:half2) = corner1;
mult(1:half1, half2+sm:ssC+sm) = corner2;
mult(half1+sm:sC+sm, 1:half2) = corner3;
mult(half1+sm:sC+sm, half2+sm:ssC+sm) = corner4;
mult(half1:(half1+sm), half2:(half2+sm)) = middle;

figure;
surf (mult, 'LineStyle', 'none');
shading interp
title ('window function');

%extending truncated convolved signal

l = ceil(.5*(length(mult)-length(I2)));
I2ext = wextend(2, 'spd', I2,l);

figure;
subplot (3,3,[1,4,7]);
surf(I2, 'LineStyle', 'none');
colormap(hsv);
shading interp
title('truncated convolved signal');
subplot (3,3,[2,5,8]);
surf (I2ext, 'LineStyle', 'none');
shading interp
title ('convolved signal extended');

[sm1,sm2] = size(mult);

%multiply extended signal by window
if length(mult)==length(I2ext)
I2extwin = mult.*I2ext;
else I2extwin = mult.*I2ext(1:sm1,1:sm2);
end
%
subplot (3,3,[3,6,9])
surf(I2extwin, 'LineStyle', 'none');
shading interp
title('mult by window');

[sI2,sI22] = size(I2extwin);
[sG,sG2] = size(G);

```

```

%begin deconvolution

G(25,25) = 2.5*G(25,25);

IT = fft2(I2extwin);
GT = fft2(G,sI2,sI22);
FT = IT./GT;
f2 = ifftn(FT);

%fixing shift
window = p/2;
shifted = ceil((window-trunc)*sG);
[sf2,ssf2] = size(f2);

if shifted > 1
f3=f2(shifted+2:sF+shifted+2, shifted+2:sF+shifted+2);
else if shifted == 0;
    f3 = f2;
else
    f3(1:abs(shifted)-1, abs(shifted):sF+abs(shifted)-1)=
f2(sf2+shifted+2:ssf2, 1:sF);
    f3(abs(shifted):sF+abs(shifted)-1, 1:abs(shifted)-1)= f2(1:sF,
ssf2+shifted+2:ssf2);
    f3(1:abs(shifted)-1,1:abs(shifted)-1)=f2(sf2+shifted+2:sf2,
ssf2+shifted+2:ssf2);
    f3(abs(shifted):sF+abs(shifted)-1,abs(shifted):sF+abs(shifted)-1) =
f2(1:sF,1:sF);
    end
end

t3 = trapz(f3);
s3 = sum(t3);

f3 = f3/s3;

figure;
surf(f3);
colormap(hsv);
title('deconvolved signal');

f3 = f3(1:sF,1:ssF);

%plot of true, convolved, deconvolved signals

figure;
subplot (3,3,[1,4,7], 'replace');
imagesc(f)
axis tight
title('true signal','LineStyle','none');
shading interp
set(gca, 'nextplot', 'replacechildren');

```

```
subplot (3,3,[2,5,8], 'replace');
imagesc(I2)
axis tight
title('observed signal', 'LineStyle', 'none');
shading interp

subplot (3,3,[3,6,9], 'replace');
imagesc(f3);
axis tight
title ('deconvolved signal', 'LineStyle', 'none');
shading interp
```